Polycaprolactone/Graphene Oxide–Silver Nanocomposite: A Multifunctional Agent for Biomedical Applications

Anjumol Joy[1] · Gayathri Unnikrishnan[1] · M. Megha[1] · M. Haris[1] · Jibu Thomas[2] · Elayaraja Kolanthai[3] · Senthilkumar Muthuswamy[1]

Abstract

In recent times, the global demand for multi-biofunctional tissue scaffolds is rising gradually. The present study deals with the development of multifunctional biodegradable nanocomposites obtained by reinforcing PCL with silver–graphene oxide (Ag–GO) nanohybrid with promising optical, mechanical and antibacterial attributes along with better biomineralization. Herein, we proposed a facile and effectual methodology to embed AgNPs over GO sheets via modified Hummer's and in-situ approaches, without causing any reduction in the functional groups of GO. The attachment of AgNPs on the GO surface was validated using XRD, FTIR, XPS, Raman and EDAX analyses. The uniform deposition of spherical AgNPs throughout the graphene surface was ascertained by the SEM and TEM imaging techniques. Additionally, the optical aspects of the as-prepared Ag–GO nanohybrid were investigated by UV–Vis and PL analyses, where the nanohybrid displayed enhanced photoluminescence which could be attributed to the synergetic effect of the surface plasmon resonance of Ag nanoparticles and the intrinsic luminescence of GO. Then, the incorporation of these nanoparticles into the PCL matrix considerably enhanced the luminescent nature, mechanical strength and surface wettability of the nanocomposite. The PCL/GO–Ag nanocomposites also displayed an excellent antibacterial efficiency towards *S. aureus* and *E. coli*, when compared to that of the pure PCL and PCL/GO films, because of the combined effect of bacterial membrane puncturing by GO and the release of silver ions. Further, a significant degradation rate was noted for PCL/GO–Ag nanocomposites with better biomineralization. So, Ag–GO nanohybrid act as a potent nanofiller for making a multifunctional nanocomposite with luminescence, better hydrophilicity, improved mechanical strength, high antibacterial property and effectual bioactivity which aids in developing a versatile tool for applications in biomedical field.

✉ Elayaraja Kolanthai
mkeraja@gmail.com

✉ Senthilkumar Muthuswamy
msenthilkumar818@gmail.com

1 Department of Physics, Karunya Institute of Technology and Sciences, Coimbatore, India

2 Department of Biotechnology, Karunya Institute of Technology and Sciences, Coimbatore, India

3 Department of Materials Sciences and Engineering, Advanced Materials Processing and Analysis Centre, University of Central Florida, Orlando, FL, USA

Graphical Abstract
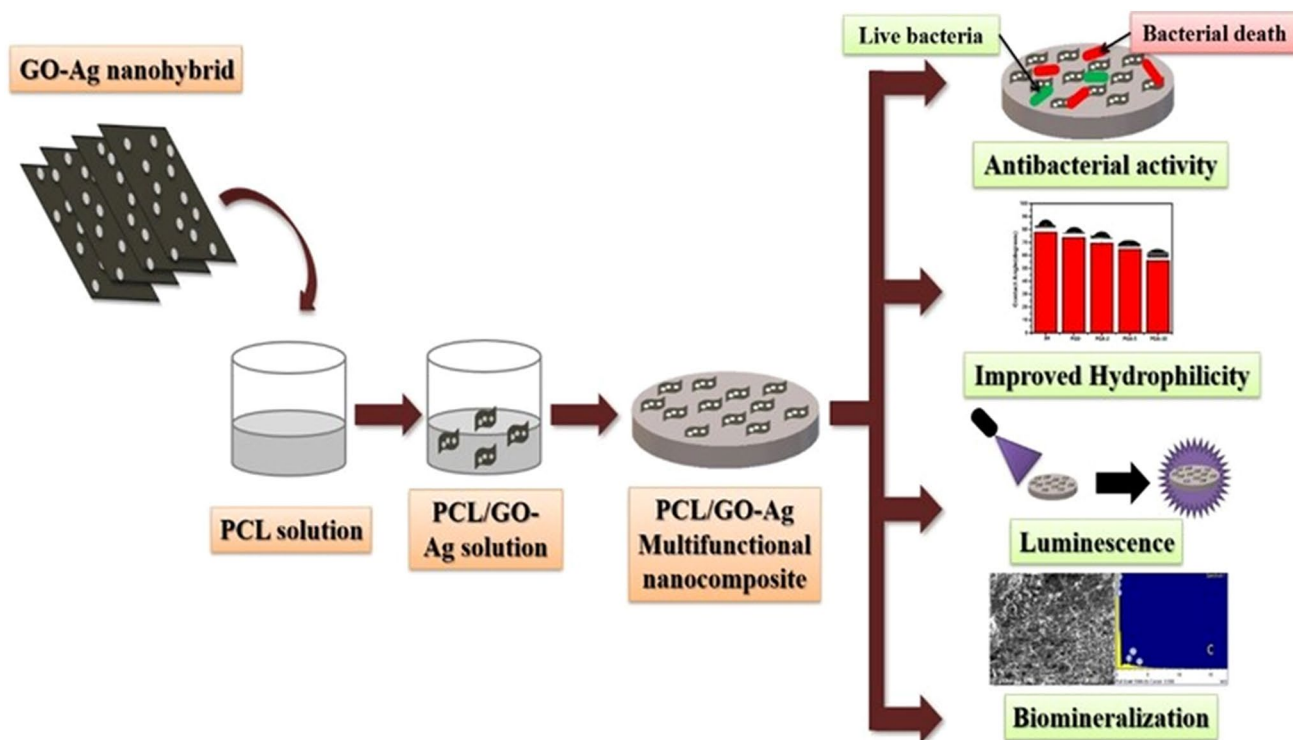
1 Introduction

Multifunctional biomaterials are said to be a rising exigency for the betterment of the biomedical field globally. For instance, they are employed in say drug or gene delivery, biological sensing, tissue engineering and molecular imaging [1–5]. An extensive range of synthetic and natural polymers are utilized as biomaterials [6]. While the benign nature of these polymers makes them suitable for the biological platform, the absence of specific physical characteristics tends to diminish the response to biological systems. Such polymers are liable towards bacterial growth and subsequent infection, which might engender malfunctioning of implantable devices. Various kinds of antibiotics and drugs are introduced to these materials to ward-off these implant-related complications. Nevertheless, most of the drugs are exorbitant and possess serious after-effects [7]. Therefore, incorporating nanoparticles into the polymer matrix offers a strategy to augment the preferred. Since, a tremendous demand was found for nanomaterials because of their large surface to volume ratio on account of its nano-sized dimensions [8–12] as well as their feasibility in interacting with live cells. Recent research focuses on tailoring one or more

suchlike nanoparticles which could acquire distinguished properties [13–18]. The advent of nanohybrids have enabled appealing and innovative methods of developing multifunctional nanocomposites [19–22].

Amongst numerous biodegradable polymers, Polycaprolactone (PCL) is well-known for its conspicuous properties like non-toxicity, good in vivo bioresorbability, outstanding biocompatibility, excellent spinnability and biodegradation without toxic end-products [23–25]. Therefore, PCL is befit for the preparation of biodegradable scaffolds as well as for the implants used for the resorbable rupture fixing. Nevertheless, the ductile PCL is habitually prone to bacterial fouling, owing to its weak inherent antibacterial efficiency, and also its poor mechanical strength impede their application in biomedical domain [26]. In consequence, diverse techniques including amalgamation of two or more biopolymers [27], surface functionalization [28] and inclusion of nanofillers [29], are being established for enhancing the polymer characteristics. Among these techniques, PCL incorporated with assorted fillers are being explored for improvising their characteristics, in order to develop multifunctional biodegradable nanocomposites. In the study by Nirmala et al., silver loaded hydroxyapatite was added into PCL matrix

which exhibited excellent cell adhesion and proliferation, and also noticeable mechanical and thermal behaviour [30, 31]. Likewise, Santis et al. incorporated iron/hydroxyapatite nanoparticles into PCL system and a notable enhancement was observed in their biological, magnetic and mechanical behaviours. Improved cell adhesion and mineralization over the iron/hydroxyapatite doped PCL matrix was ascertained via in vivo and in vitro methods, which could be ascribed to the synergistic action of iron/hydroxyapatite nanohybrid [32].

Recently, metal oxide and metal adorned graphene oxide (GO) nanoparticles are finding wide range of applications in biological systems [33–35]. The arising attention toward these nanohybrids come about due to the synergistic action of the elemental nanoparticles, which bring about exceptional characteristics in them. GO holds admirable physical and biological behaviour, as well as particularly larger surface area [36–38]. Li et al. proposed GO incorporated hydroxyapatite as a biomimetic nanohybrid with exceptional mechanical strength as well as improved biocompatibility [39]. When GO is incorporated into PCL framework, the biophysical properties such as mechanical strength, hydrophilicity and antibacterial efficacy, are said to amplify at minimal concentrations [40, 41]. Mechanically enriched nanocomposite could be exploited for applications like the development of artificial bone grafts. Additionally, the antibacterial activity of GO-based nanoparticles have been studied, which could be ascribed to the mechanisms of either puncturing the bacterial cell membrane or by generating ROS [42, 43]. Yet, antibacterial agents are often made use of, to uplift the nominal intrinsic antimicrobial property of GO [44].

Metal nanoparticles act as a prominent factor in inhibiting the infection caused by the bacterial growth, on account of their size and shape-related properties and also its larger surface area [45, 46]. Among them, Silver nanoparticles (AgNPs) exhibit excellent antibacterial activity without the release of toxic biocides, and as a result, AgNPs are counted as environment-friendly and non-toxic materials for biomedical applications [47–49]. The promising antibacterial and antioxidant performances along with the cytotoxicity against HepG2 cell lines of AgNPs were investigated by Das et al., and validated the vital role of AgNPs in biological system [50]. The self-luminescence and antibacterial property of AgNPs makes it a potential candidate which can be used as antibacterial agents, and also for imaging and tracking. As it is a difficult task to disperse AgNPs in the PCL matrix, it is vital to use surfactants in order to minimalize its aggregation. This surface functionalization is capable of hindering the Ag^+ ion release and also exhibit cytotoxicity [7]. Recent studies show that silver decorated GO proffers many exciting characteristics. For instance, silver nanoparticles tend to prevent restacking and aggregation between graphene sheets. Also, the sheets of

graphene perform as an authentication for the stabilization of silver nanoparticles, inhibiting the aggregation and promoting dispersivity [51]. In a work by Shao et al., the decoration of silver NPs on GO showed an enhancement in the antibacterial activity of Ag–GO when compared to Ag and GO nanoparticles individually [52]. In another work by Javad et al., AgNPs were ornamented over the GO sheets, and it exhibited excellent mechanical and antibacterial properties due to the synergistic actions of GO and AgNPs [53]. While extensive studies have been done on the suspension of Ag–GO nanoparticles, their practicality in the construction of polymer nanocomposite is not completely investigated, especially on PCL matrix. So far, only very few works have been done based on PCL nanocomposites incorporated with graphene-Ag nanohybrid [51, 54, 55]. Kumar et al. utilized PCL/rGO–Ag nanocomposite for tissue engineering applications [51] and also, Pan et al. developed an antibacterial polymeric mat comprising of PCL, rGO and AgNPs against *S. aureus* and *E. coli* [55]. The bioactivity and mechanical performance of GO, when compared to that of rGO, is quite commendable in PCL matrix. In the work done by Kumar et al., GO imparts an increment in the strength and modulus as well as enhanced surface wettability rather than rGO, when incorporated into PCL system [56]. Shahmoradi et al. introduced GO/Ag/Arginine nanoparticle system into PCL matrix which exhibited significant angiogenesis along with antibacterial activity for wound healing applications [54]. So, extensive studies on the feasibility of Ag–GO in polymer nanocomposites for bone tissue engineering applications are required along with that of rGO–Ag, since the presence of immense functional moieties in GO benefits in the augmentation of its bioactivity.

Based on the above mentioned points, we centered our work on the utilization of Ag–GO nanohybrid for the fabrication of polymer-based nanocomposites with improved nanoparticle dispersivity. In our work, we present a facile and effectual method for anchoring AgNPs over GO surface, where GO was synthesized by the modified Hummer's technique and AgNPs were embedded over GO via in-situ growth technique, without causing any reduction in the functional groups of GO. In addition, PCL was employed as a platform for the synthesis of nanoparticle incorporated composites. The physicochemical and biological properties of various nanocomposites were investigated to validate the distinctive aspects of our nanohybrid, which is capable of imparting multifunctional attributes to the polymer matrix.

2 Materials and Methods

2.1 Materials

Graphite flakes (99% purity, Superior Company), potassium permanganate (KMnO$_4$, ≥99%, Sigma Aldrich),

sulphuric acid (H$_2$SO$_4$, 98%, Sigma Aldrich), orthophosphoric acid (H$_3$PO$_4$, 99.99%, Sigma Aldrich), hydrochloric acid (HCl, ACS reagent, 37%, Sigma Aldrich), hydrogen peroxide (H$_2$O$_2$, 35 wt%, Sigma Aldrich), silver nitrate (AgNO$_3$, 99.0%, ACS reagent, Sigma Aldrich), NaOH pellets (99.99%, Sigma Aldrich), Polycaprolactone (PCL; M$_n$ = 80,000 gmol^{-1}, Sigma Aldrich), Tetrahydrofuran (THF, 99.9%, Sigma Aldrich) and Phosphate Buffered Saline solution (PBS, pH = 7.4, SRL) were procured and used without any additional purification. Deionized (Millipore) water was used for all the experiments.

2.2 GO Synthesis by Chemical Oxidation Method

The synthesis of nanolayer of GO was carried out via a modified Hummer's method using graphite flakes [56, 57]. In brief, a mixture of sulphuric acid and orthophosphoric acid (55:7) was taken in a 1 L beaker and graphite (1 g) powder was added slowly into it. Subsequently, 5.6 g of KMnO$_4$, as an oxidizing agent, was added sluggishly to increase the oxidation rate. The resultant mixture was stirred using a magnetic stir bar under constant speed (400 rpm) for 72 h at room temperature, for the oxidization of the graphite flakes. Further, to stop the oxidation, H$_2$O$_2$ solution was added drop wise until the color changed from brownish-black to a yellowish solution. The resulting solution was then subjected to a cleaning process in which 1 M HCl and distilled water were used alternatively. After centrifuging the solution at 5000 rpm for 30 min and drying at 40 °C under vacuum condition for 3 days, the GO particles were collected from the solution.

2.3 Synthesis of Silver Decorated GO

Initially, 2.5 mg ml^{-1} of GO was disseminated in de-ionized water using an ultra-bath sonicator, for 2 h followed by probe-sonication procedure was carried out for 1 h in an ice-bath (4 °C) to make a uniform dispersion. The resultant GO stock solution was maintained at 4 °C until further use for experiments. Silver decorated GO was synthesized in a one-step reaction via reducing AgNO$_3$ in GO dispersion. From the stock solution, 50 ml GO was added into a 100 ml three-neck flask and was kept for boiling condition. The temperature was allowed to reach at 80 °C and, a suitable amount of AgNO$_3$ solution (5 wt%, 3 wt%, 1 wt%) was slowly added to the mixture under an inert atmosphere using argon gas. After continuous stirring for 3 h, NaOH solution was rapidly added into the mixture and it was boiled again for 3 h. Finally, Ag–GO nanoparticles were centrifuged at 30,000 rpm for 45 min and dried at 60 °C under vacuum condition for 15 h to obtain GO–5Ag, GO–3Ag and GO–1Ag.

2.4 Synthesis of PCL/GO-Ag Nanocomposites

Pure and nanoparticle incorporated PCL films were prepared by the solvent casting method (Fig. 1) and Table 1 enlists the acronyms of the samples and their corresponding compositions. Firstly, pure GO, GO–1Ag, GO–3Ag and GO–5Ag were dispersed separately, in THF using magnetic stirrer for 24 h. Later, PCL beads (0.1 g ml^{-1}) were added into the nanoparticle dispersions and again stirred for 24 h, for obtaining homogeneous solution. The concentration of GO, GO–1Ag, GO–3Ag and GO–5Ag
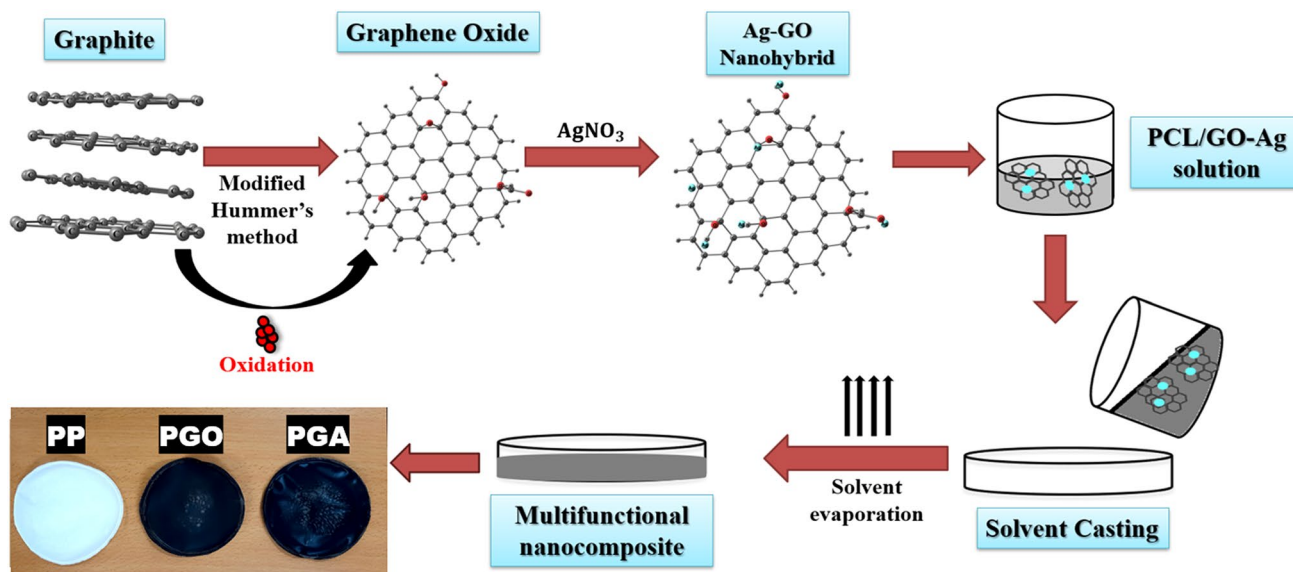

Fig. 1 A schematic on preparation route of GO, Ag–GO nanohybrid and multifunctional PCL/GO–Ag nanocomposite

Table 1 The composition and nomenclature of the as-synthesized polymer composites

Sample code	Sample composition
PP	Pure PCL
PGO	GO incorporated PCL
PGA-1	1 wt% Ag doped GO in PCL
PGA-3	3 wt% Ag doped GO in PCL
PGA-5	5 wt% Ag doped GO in PCL

were taken to be 5% of PCL. And in the case of Ag–GO nanohybrid, the strategic weight percentages of the Ag nanoparticles on GO were considered. So, surplus amount of Ag–GO were taken when compared to pure GO, for maintaining the same amount of GO in the polymer. The resultant solutions were molded into polymer films (PGO, PGA-1, PGA-3 and PGA-5) via solvent casting method and the films were dried at room temperature. For the preparation of pure PCL film (PP), the same procedure as above was followed, without the addition of nanoparticles. Figure 1 shows a schematic representation of the synthesis of polymer nanocomposites and their application.

Thus, the synthesis of PCL/GO–Ag nanocomposites comprises two steps: first, the preparation of the Ag–GO nanohybrid and second, its incorporation into the PCL matrix. In the Ag–GO nanohybrid, the spectroscopic results provide information on the formation of Ag^0 NPs and not the formation of Ag^+ complexes with the GO. It means that the AgNPs were physically adsorbed to the GO sheets. It follows that the composite involves a simple dipolar interaction and not covalent bonding. It can be perceived that the AgNPs are distributed throughout the GO layer as any aggregation in a confined area would lead to a change of absorption wavelength by a significant extent than the actual observed shift. Further information on the contribution of various elements are provided in the discussion on XPS spectra. These AgNPs over the GO sheet surface act as spacers which makes the adjacent GO sheets separate and help in preventing restacking or aggregation of the sheets [58]. As a result, well exfoliated GO sheets with uniformly decorated AgNPs were obtained and were used as effective nanofillers in the PCL system to enhance the mechanical behaviour, surface wettability, antibacterial efficacy and biomineralization of the polymer. The presence of oxygen rich functional groups improves the dispersivity of the exfoliated GO sheets adorned with metallic AgNPs and results in its strong interaction with the polymer, which results in the formation of PCL/GO–Ag nanocomposite. Accordingly, the physical and biological properties of the polymeric nanocomposites are enhanced. Also, the wrinkled curves on the GO surface increased its interlocking with the polymer matrix [59].

2.5 Characterizations

The morphologies and elemental compositions of Ag–GO nanohybrids and PCL nanocomposites, were analyzed using a scanning electron microscope (Jeol Japan-6390) along with EDAX and HR-TEM (Jeol-2100+). The diffraction patterns of GO, Ag–GO and PCL nanocomposites were detected via automated X-ray diffractometer (XRD-6000 Shimadzu, Japan), employing a CuKα monochromatic radiation with an execution voltage of 40 kV, λ = 1.54056 Å, 40 mA operating current, and a scanning rate of 5° min⁻¹. The anchored functional groups over GO and the as-synthesized Ag–GO nanohybrid were examined by the Fourier-transform infrared spectroscopy (FTIR). The samples were combined with KBr and then converted to pellets, and a spectrum between 500 and 4000 cm⁻¹ was noted using a Shimadzu prestige-21 FT-IR instrument. He-Ne laser with excitation wavelength 633 nm was used for Raman measurement. A JASCO V-770 spectrophotometer was used to record UV–Vis absorption spectra in the range of 300–800 nm. The photoluminescence spectra of Ag–GO nanohybrid and PCL nanocomposites were determined using a Fluorolog, Horiba Jobin Yvon spectrophotometer, with a He-Cd laser source. The dispersibility states of AgNPs, GO and Ag–GO nanohybrid were evaluated in THF by ultra-sonicating it for 2 h, and the dispersions were kept unruffled for an hour at room temperature. The hydrophilic behaviour of all PCL films were assessed by automated contact angle goniometer (290-U1, RAME-HART). Deionised water was utilized for the Sessile droplet contact angle measurement, where the reported angles cover the average of 10 individual measurements. The mechanical attributes of the PCL nanocomposites were measured using computerized universal testing machine (CUTM-50KN), in consonance with the ASTM standards.

The method of immersion was followed in order to analyze the influence of the nanohybrid on the degradation rate of casted PCL films. All the samples (in triplicates) were submerged in 2 ml of phosphate buffer saline (PBS) solution and incubated at room temperature for 6, 12, 18 and 24 days. The films were taken out, dried in vaccum and weighed, on the decided days. The reduction in the mass (in %) of different polymer films was evaluated by the following equation:

$$\text{Mass loss (in \%)} = \frac{M_0 - M_t}{M_0} \times 100 \qquad (1)$$

where, M_0 represents the initial mass of the film prior to degradation in buffer and M_t represents the mass of the film at different times. The antibacterial activity of the PCL nanocomposites were investigated against *E. coli* (gram-negative) and *S. aureus* (gram-positive) through the disk-diffusion assay. The experimental section involved two distinct batches (n = 3) for *E. coli* and *S. aureus*, and their

average value was considered. For evaluating the extent of biomineralization of the polymer films (PP, PGO, PGA-1, PGA-3, PGA-5), they were soaked in SBF (simulated body fluid) solution. After a period of 15 days, the samples were vaccum dried and examined by SEM and EDAX analyses for confirming the formation of apatite over its surfaces.

3 Results and Discussion

3.1 Characterization of Nanohybrid Materials

3.1.1 Morphological and Elemental Analyses

The surface morphology and compositional analysis of GO and Ag decorated GO with different concentrations of Ag are shown in Fig. 2. The SEM micrograph of GO reveals the characteristic lamellar structures and the layered morphology having curves and wrinkles. The exfoliated GO sheets have coupled with each other, forming thick layers owing to the presence of oxygen functional groups [60]. After decorating Ag over GO sheets, spherical shaped silver nanoparticles homogenously deposited on the GO surface were noticed and none of the particles were located beyond the GO sheets. Here, the GO sheets act as both negatively charged surface for arresting Ag^+ ions, as well as a supporting platform for reducing Ag^+ ions to AgNPs [61]. Furthermore, the Ag nanoparticles perform as spacers which make the adjacent GO sheets separate [62]. Besides, no variations were detected in the lamellar structure of hydrophilic GO even after the silver attachment on to it. Also, the Ag concentration affects the size and shape of silver nanoparticles present in GO. At lower concentrations (GO–1Ag), the detection of silver deposition on the GO sheet is difficult. As the doping concentration increases (GO–3Ag, GO–5Ag), the size of silver nanoparticles also increases and its deposition
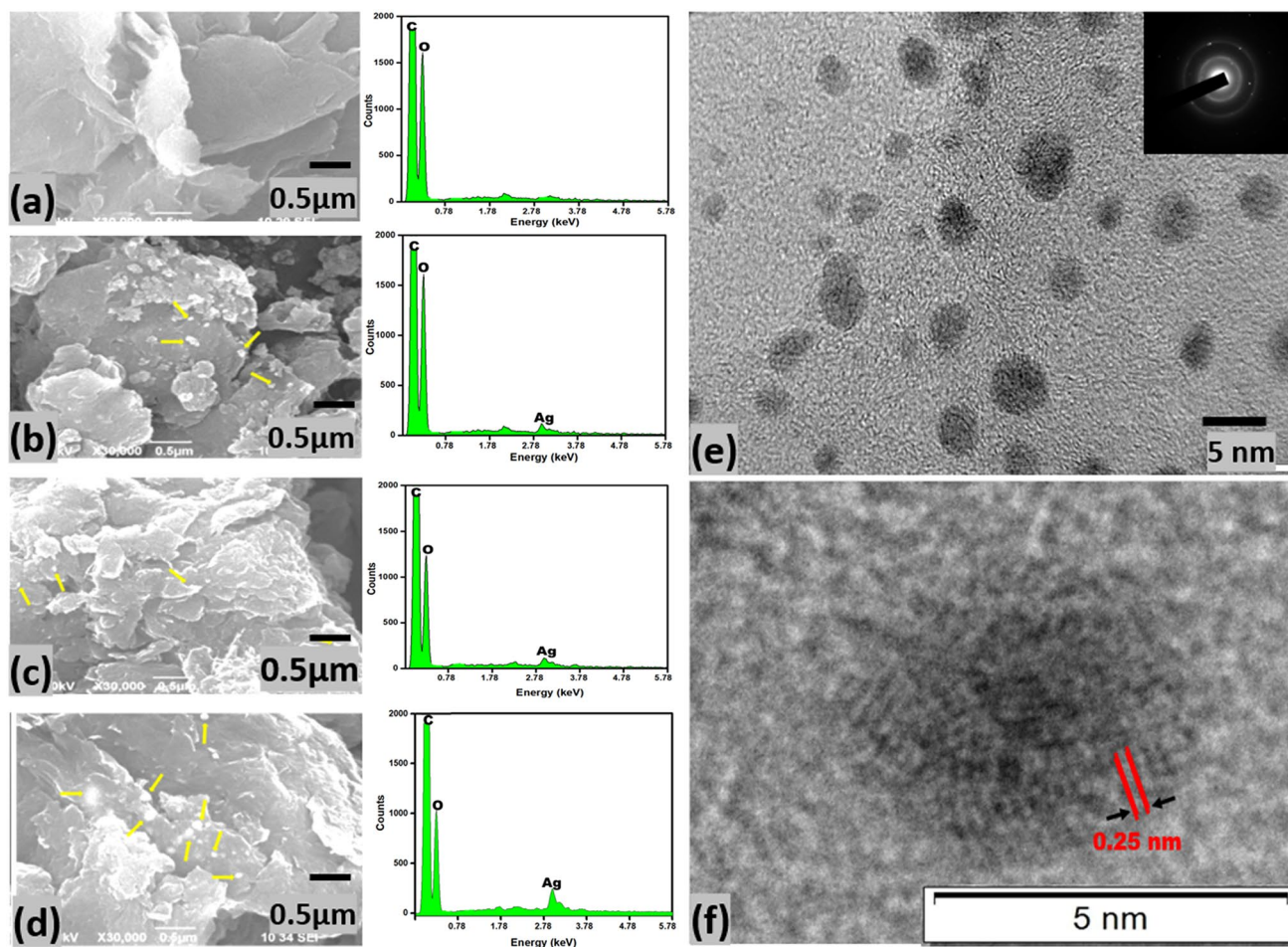

Fig. 2 SEM micrographs of synthesized pure GO and Ag incorporated GO with different concentrations (arrows indicate Ag nanoparticles) and their corresponding EDAX analysis **a** GO, **b** GO– 1Ag, **c** GO–3Ag, **d** GO–5Ag. **e** and **f** display the TEM micrographs and SAED pattern (inset) of GO–5Ag
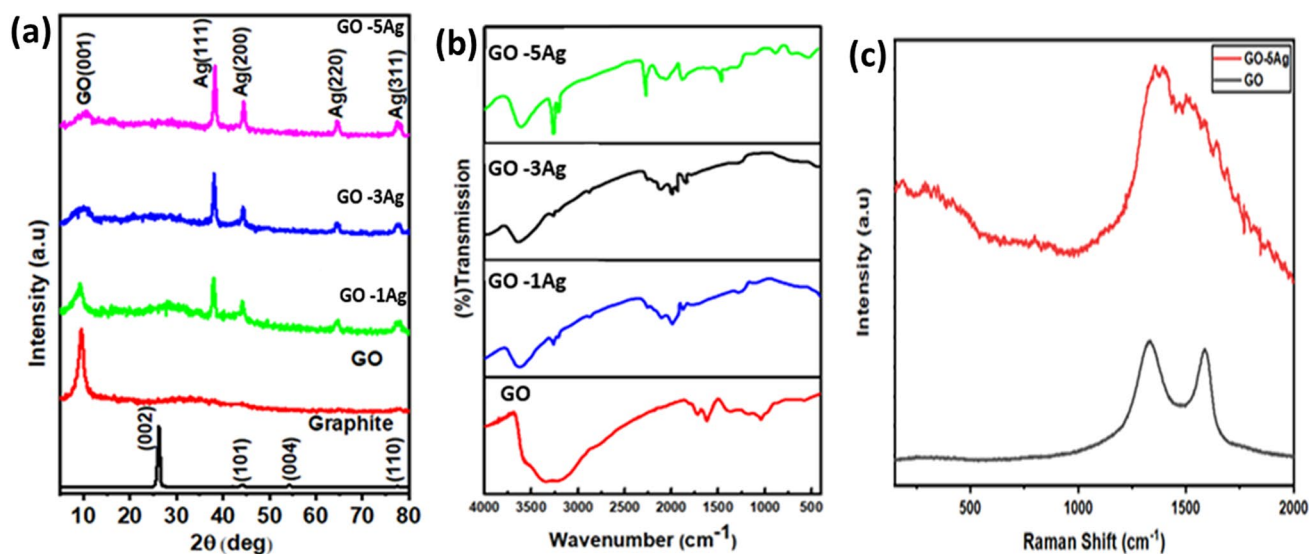
Fig. 3 **a** X-ray diffraction (XRD) patterns of pure graphite, graphene oxide and Ag doped graphene oxide: (Graphite) commercially available graphite,(GO) synthesized graphene oxide, (GO–1Ag) is 1 wt% Ag doped GO, (GO–3Ag) is 3 wt% Ag doped GO and (GO–5Ag) is 5 wt% Ag doped GO. **b** FTIR spectrum of pure and hybrid nanoparticles: different samples: (GO) Hummer's method synthesized graphene oxide, (GO–2Ag) is 1 wt% Ag doped GO, (GO–3Ag) is 3 wt% Ag doped GO and (GO–5Ag) is 5 wt% Ag doped GO. **c** Typical Raman spectra of synthesized pure and hybrid nanoparticles, (GO) the pure form of graphene oxide and (GO–5Ag) is 5 wt% Ag doped GO

is visible on GO sheets (Fig. 3c, d). The EDAX plots of Ag–GO nanoparticles attest the presence of Ag along with C and O. Therefore, the results indicate the successful anchoring of Ag nanoparticles on the GO surface.

As noticed from the typical TEM micrographs (Fig. 2e), the adhesion of spherical AgNPs over the GO sheet surface is evidently perceptible, and its highly magnified image (Fig. 2f) elucidate the characteristic interplanar d-spacing value of 0.25 nm for AgNPs, concordant with their crystal plane (111). Also, the SAED pattern of Ag–GO nanohybrid (inset of Fig. 2e) portrays bright spots and diffraction rings which could be assigned to the FCC structure of AgNPs, and the corresponding rings accord with the (111), (200), (220), and (311) crystalline planes of silver. Thus, the procured results signify the polycrystalline structure of AgNPs and are also in good accordance with the XRD data.

3.1.2 XRD

Figure 3a gives the structural information of graphite, graphene oxide (GO), and Ag–GO nanohybrid using XRD analysis. Graphite shows a strong diffraction peak at $2\theta = 26.2°$ (002) and a minor peak at $2\theta = 77.6°$ (110), which indicates the pure phase of the material (JCPDS No. 41-1487). By Bragg equation ($2d\sin\theta = \lambda$), the obtained inter-planar d-spacing of graphite is 0.34007 nm. Nevertheless, GO shows a narrow and sharp diffraction peak ($2\theta = 9.5°$) with an inter-planer d-spacing of 0.9279 nm, which is a characteristic feature of (001) plane. The obtained increment in the d-spacing

value indicates the raise in occurrence of the functional moieties (epoxide, carboxyl, and phenolic) between graphene layers, when graphite is oxidized in the highly acidic medium [56]. In Ag–GO, the observed peaks at 38.1°, 44.3°, 64.6°, and 77.7° can be attributed to the planes (111), (200), (220), and (311) respectively, which are in accordance with FCC Ag (JCPDS Card No. 65-2871).The prominent peak spotted at 38.1° corresponds to pure crystalline Ag nanoparticles, which authorizes that the nanohybrid comprises of Ag nanoparticles in pure crystalline form [63]. Also, the peak intensity of Ag was enhanced when the percentage of incorporation of AgNPs was varied from 1 to 5%, which attests that a greater number of Ag nanoparticles are decorated over the graphene surface. The anchoring of AgNPs on graphene surface aids in minimizing the restacking of GO sheets, which is apparent through the reduction in the intensity of GO peak [64]. From earlier literature, it has been revealed that the attenuation of GO peaks, owes to reduced restacking of GO sheets, subsequent to the addition of metallic nanoparticles [65]. Thus the attained outcomes attest that GO–5Ag with minimal GO peak, exhibits effectual exfoliation.

3.1.3 Fourier-Transform Infrared Spectroscopy

Figure 3b depicts the FTIR spectra of GO and Ag–GO nanohybrid (GO–1Ag, GO–3Ag, GO–5Ag). Considering GO, a broad and intense absorption band between 3600 cm^{-1} and 2800 cm^{-1} was obtained which points the stretching vibrations of O-H from the hydroxyl group surface [66]. And a

peak at 1718 cm^{-1} relates to the C=O stretching vibrations in carboxylic moieties mounted at the edges of graphene sheets [56]. The peak at 1631 cm^{-1} denotes the C=C skeletal vibration of aromatic carbon or intramolecular hydrogen bonds of unoxidized graphitic domains [51]. In addition, 1046 cm^{-1}, 1209 cm^{-1}, and 1382 cm^{-1} peaks indicate C−O stretching vibrations, C-O-C stretching, and C−O−H deformation respectively [52]. The acquired peaks validate the abundance of functional groups comprising oxygen, which aids GO to be suitable for further modification with plasmonic nanoparticles, like silver. After decorating Ag on GO sheets, some characteristic peak shifts were noted. Also, the peak intensity of hydroxyl moieties were diminished abruptly in Ag–GO nanohybrid. These outcomes reveal the strong interactions amongst functional moeities and silver ions [67]. Additionally, the peak position and peak intensity of C=O groups were varied significantly, which affirms the formation of coordination bond due to the interaction amid C=O groups and silver ions [67]. Also, the peaks corresponding to the groups of C–O and C–O–C, altered the absorption features. The perceived peak shift and intensity deviation elucidate that the functional groups comprising oxygen permit appropriate anchoring of AgNPs over graphene surface. Thus, FTIR results corroborate the XRD data, indicating the successful exfoliation of GO and attachment of Ag over the GO surface.

3.1.4 Raman Spectra Analysis

The GO and silver incorporated GO were characterized by Raman spectroscopy and Fig. 3c show the attained results. The Raman spectrum of GO reveals two bands at about 1590 cm^{-1} and 1327 cm^{-1}, analogous to the graphitic (G) and diamondoid (D) bands, respectively [68]. Likewise, in Ag–GO nanohybrid, two distinctive bands at 1395 cm^{-1} (D band) and at 1529 cm^{-1} (G band) were noted. Resulting from the vibrations of hybrid C atoms, the D-band asserts the C ring breathing mode, which might be considered as the structural defect of graphene, while the G-band is deriving from the C–C bonds stretching vibration [69]. Furthermore, the enriched Raman peak intensities of the G-band and D-band for Ag–GO nanohybrid, owes to the SERS offered by local electromagnetic fields generated by silver nanoparticles, accompanied by the plasmon resonance [62]. Moreover, it was witnessed that the D peak intensity was more than that of the G peak for Ag–GO nanohybrid, which could be accredited to a rise in defect concentration [70]. Thus, the perceived spectra substantiate the effectual decoration of AgNPs on the graphene surface.

3.1.5 XPS Analysis

Figure 4 depict the XPS spectra of various elements that are components of the Ag–GO nanohybrid. The deconvoluted spectrum of carbon (Fig. 4b) reveals the C–O carbon peak at 286.3 eV. The 1s electron peaks of C corresponding to the sp^2 hybridized state at 284.5 eV and the O–C=O at 288.9 eV imply the presence of graphene in its oxidized form [71]. The 1s electrons of oxygen are present in O^{2-} state mainly, as shown by the 530.9 eV peak (Fig. 4c). It occupies a major portion of the XPS spectrum. The XPS peaks of oxygen further confirm the GO formation. In addition to the evidence on the GO structure, the presence of Ag in the nanohybrid is evidenced by the XPS peaks of Ag. The Ag 3d$_{3/2}$ and 3d$_{5/2}$ states are observed at 368.7 eV and 374.7 eV respectively (Fig. 4d). These peaks reveal that they arise from the electronic states of the elemental Ag [61]. Since the contribution by Ag$^+$ states are not apparent in the spectrum, it follows that the AgNPs are surrounded by the oxygen atoms of GO. The negative ions of O may lead to a chemisorbed structure around the AgNPs.

3.1.6 UV–Visible Spectroscopy

As-prepared samples were subjected to UV–Visible analysis and Fig. 5a discloses the UV–Visible absorption spectra of pure and Ag–GO nanohybrid. The $\pi \rightarrow \pi^*$ transitions of aromatic C–C bond is the foremost reason for the occurrence of the characteristic absorption peak at 230 nm [72]. The shoulder peak at about 302 nm can be attributed to the n$\rightarrow \pi^*$ transitions of C=O bonds indicating the formation of GO [73]. These achieved results corroborate the XRD and FTIR results that confirm the presence of oxygen functional groups in Ag–GO nanohybrid. In Ag–GO nanohybrid absorption spectrum, the distribution of AgNPs over GO surface was divulged by the SPR peak around 380 nm, which could also be authenticated from prior studies [52]. From the SEM results, also in accordance with the previous reports, the AgNPs seem to be spherical in shape when its absorption peak is around 400 nm. [52]. The enhanced resonance peak of GO–5Ag can be ascribed to the strong interaction amongst GO and metallic Ag.

3.1.7 Photoluminescence

The photoluminescence (PL) spectra of Ag–GO nanohybrids of varying Ag concentrations; GO–1Ag, GO–3Ag, GO–5Ag are shown in Fig. 5b. PL spectra provide information about the photo-induced transfer and recombination of electron-hole pairs in semiconductors. In GO, a very weak PL is exhibited because of the existence of oxygen-related species (e.g. epoxy and hydroxyl groups) which produce non-radiating re-combinations, due to the electron-hole (e-h)
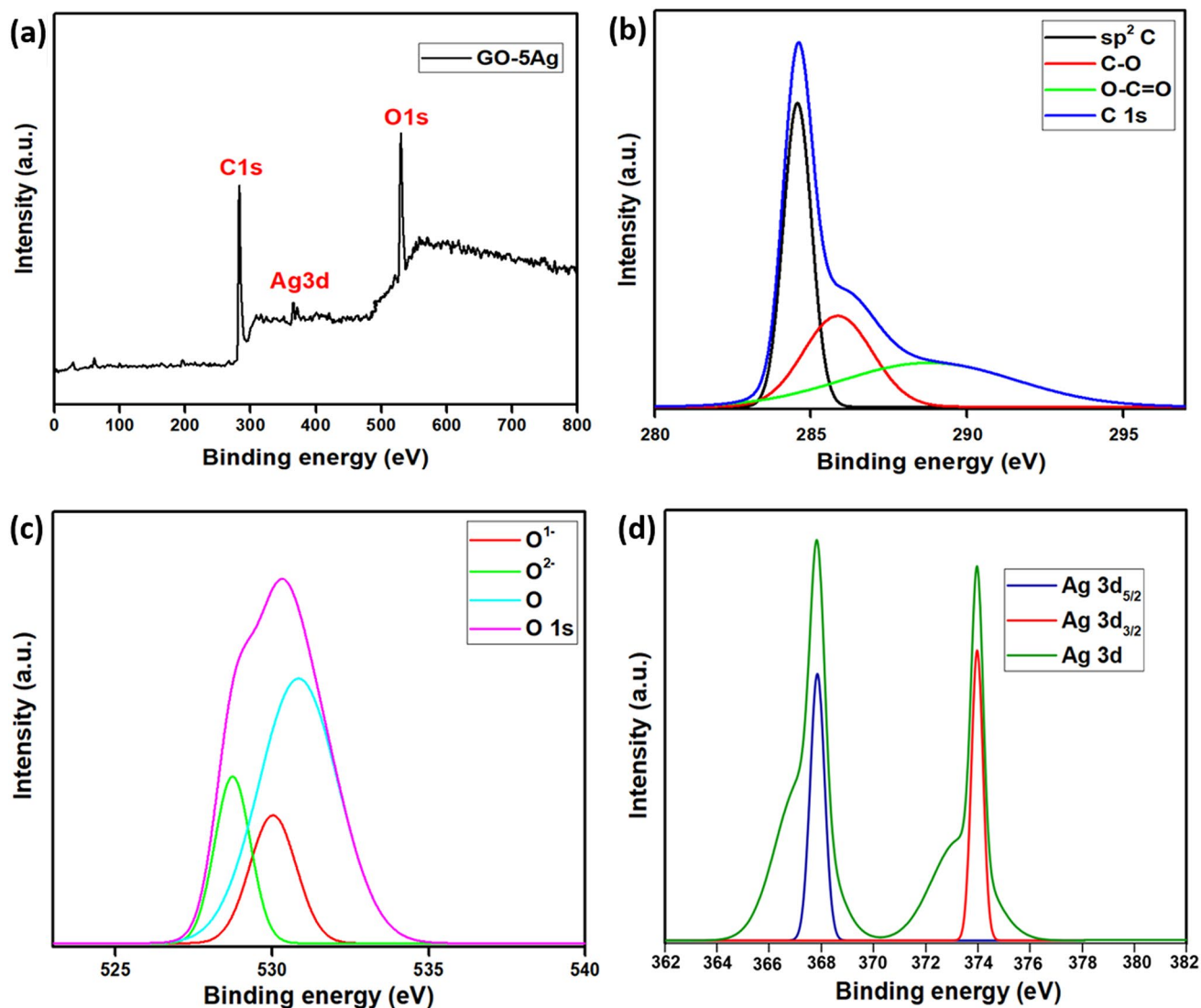
Fig. 4 **a** XPS spectrum of the as-prepared Ag–GO nanohybrid, deconvoluted XPS spectra of **b** C1s of GO nanosheet, **c** O1s of graphene nano-particles and **d** Ag 3d of Ag–GO nanohybrid

recombination in the sp^2 clusters [74]. The present study demonstrates an enhancement in photoluminescence of GO by embedding silver over its surface. In AgNPs, a promi-nent emission peak around 400 nm [75] in the visible range, could be attributed to the electron excitation from the occu-pied D bands to the bands above Fermi level [76]. The PL spectra for Ag–GO nanohybrid illustrate emission peaks at 407 nm and 430 nm for GO–1Ag, at 418 nm and 440 nm for GO–3Ag, and at 418 nm and 440 nm for GO–5Ag, which could be accredited to the interaction amid luminescence of atomically thin-layered GO and the LSPR effect from the AgNPs. The anchoring of AgNPs over GO enhances the luminescence on account of the recombination of electron-hole pair of GO and oscillating electrons of AgNPs [77]. Further, an increment in the luminescence peak intensity

was noted in accordance with the increasing concentration of AgNPs, as a consequence of LSPR effect [75].The resultant luminescence in Ag–GO nanohybrid, influence from this resonance effect of AgNPs on GO sheet can be deployed for imaging applications.

3.1.8 Dispersivity Studies

The dispersions of GO, Ag and Ag–GO nanoparticles in THF after ultrasonication are displayed in Fig. 6. The agglomerating tendency and rapid settling behaviour of Ag nanoparticles hinder their even dispersion in organic sol-vents. The exhibited cloudiness of Ag can be attributed to an incomplete dispersion in THF, and later on this turbid solution turns into a transparent solution with sedimented
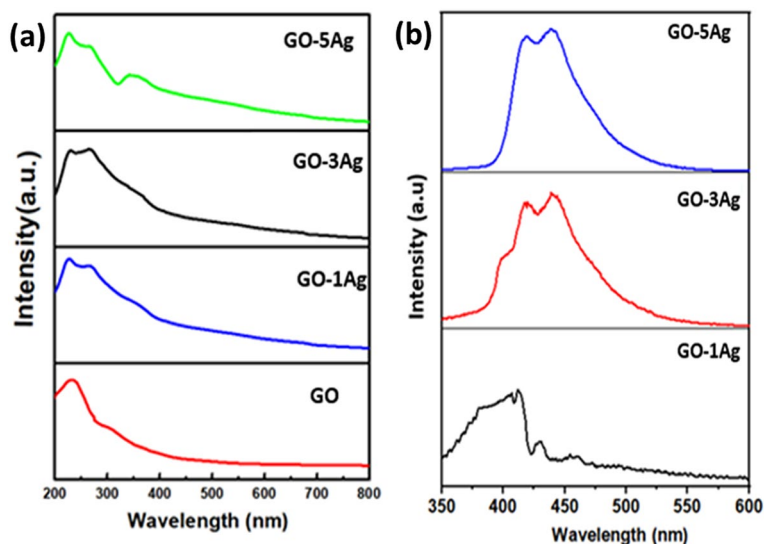
Ag nanoparticles. On the other hand, GO as well as Ag–GO revealed excellent stability and uniform dispersion in THF. The anchoring of Ag over the chemically stable GO sheets enabled it to disperse evenly into the organic solvent. Therefore, the attained stable Ag–GO nanohybrid in organic solvents can be utilized in the designing of a metal-GO-polymer nanocomposite.

3.2 Characterization of Polymer Nanocomposite

3.2.1 SEM

The surface morphologies and elemental compositions of casted pure PCL and composite films are displayed in Fig. 7. The surface mapping done by the back scattered electrons procured from the polymer surface, reveals the Ag nanoparticles as glittering spots in contrast to the dark PCL matrix. And the EDAX spectrum of PCL/GO–Ag nanocomposite

Fig. 6 The digital images of the dispersions of GO, AgNPs, and Ag–GO nanoparticles in THF

affirm the existence of Ag along with C and O (Fig. 7d). The PCL-GO film surface evinced an increase in the roughness because of the incorporation of GO nanoparticles that leads to the formation of uneven protuberance over the polymer surface, when compared to the plain PCL surface. According to the former reports, the inclusion of GO into the polymer resulted in the formation of protrusions with a wave-like morphology [78, 79], which raised the roughness of its surface and thus, is said to intensify the composite surface area [80]. In addition, the SEM micrographs substantiated the behaviour of nanoparticle dispersion in the polymer matrix [56]. Efficient adherence of GO onto the PCL surface indicated well-fused and uniform dispersion of GO nanosheets in the nanocomposite. Also, the decoration of Ag nanoparticles on the GO surface, likely prevented the formation of Ag nanoparticle aggregation which in turn aided the even dispersion of Ag–GO nanoparticles. The Ag nanoparticle growth over the GO sheet strengthens the compatibility and interactions between hydrophobic polymer matrix and hydrophilic Ag nanoparticles [51]. Thus, blending inorganic particles with stabilizers or surfactants (polymer or organic nanoparticle) boost the nanoparticle dispersivity within the polymer and enriches the nanocomposite properties [81].

3.2.2 XRD

The X-ray diffraction profiles of pure and hybrid PCL films incorporated with GO and Ag–GO are represented in the Fig. 8a. The characteristic peaks at $2\theta = 21.3°$ and $23.6°$ of pure PCL, that are consigned to the (110) and (200) planes, respectively, correspond to its crystalline orthorhombic structure and are in good accordance with the previous literature [82]. The unaffected positions of these peaks suggested that the PCL crystal structure was unaltered, even after the addition of the nanoparticles. Nevertheless, the diffraction peak of GO was suppressed
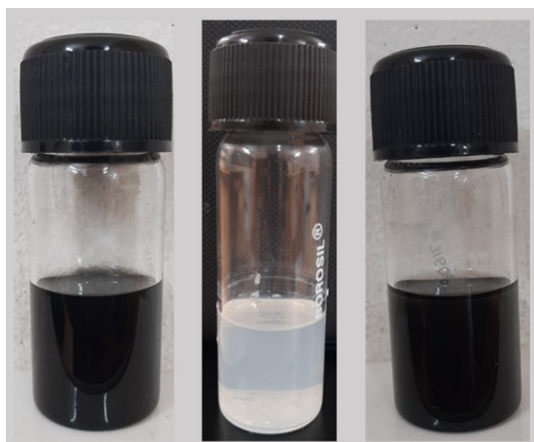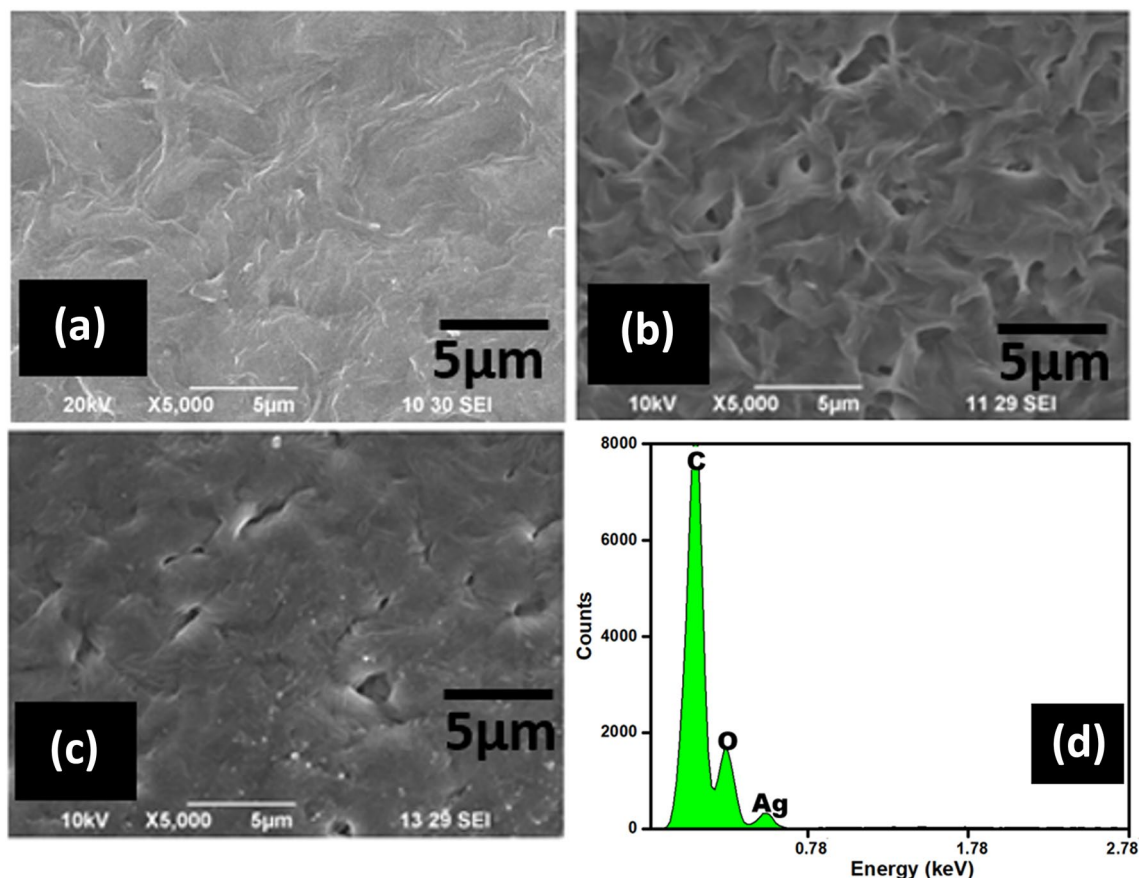
Fig. 7 Morphological and elemental analyses of pure PCL and composite films obtained by solvent casting method. SEM images of **a** Pure PCL film, **b** PCL/GO film, **c** PCL/GO–Ag film and **d** EDAX of PCL/GO–Ag film

by the strong polymer peak. The absence of GO peaks symbolizes the formation of uniformly dispersed and well exfoliated structure of GO nanosheets in the polymer matrix [83]. Thus, the inclusion of GO nanoparticles caused a minor augmentation of FWHM (full width at half maximum) of the nanocomposite peak (110), from 1.06 to 1.08. The perceived increment of FWHM of the nanocomposite could be attributed to its crystallite size reduction, in comparison to the pure PCL matrix. Earlier studies had reported that the nanoparticle dispersion could behave as a hindrance to the polymer crystal growth [84]. Therefore, the obtained results confirm that the mobility of the polymer matrix is limited by the GO dispersion, which results in the reduced crystallite size. The acquired similarity in FWHM of GO incorporated PCL peaks ((110) and (200)) suggests a constricted distribution of polymer crystal size [56]. The typical diffraction peaks corresponding to Ag were observed at 38.1° and 44.3° analogous to the planes (111) and (200) respectively, for the PCL-GO–Ag (5%) nanocomposite. This strengthens the fact that the Ag nanoparticles are reinforced into the polymer matrix and are in pure crystalline form. The broadness of the achieved Ag

peaks authenticate the existence of small—scale Ag nanoparticles [51] which is also evident in the SEM images (Fig. 7c). Hence, the integration of GO and Ag–GO into the polymer matrix is established through these X-Ray diffraction results.

3.2.3 UV–Vis Absorption

Figure 8b reveals the UV–Vis absorption spectra of pure and nanoparticle incorporated PCL films. A broader band without a distinct absorption maximum was seen. When AgNPs were incorporated (PGA-5), an additional band corresponding to AgNPs was observed. The broad absorption is not observed in the case of pure PCL (PP). The broadening of the spectra of PGA-1, PGA-3, and PGA-5 suggest that the energy states of Ag, GO and the polymer coalesce. It enables the excitation of the samples over a range of wavelengths in the UV–Vis-NIR region.
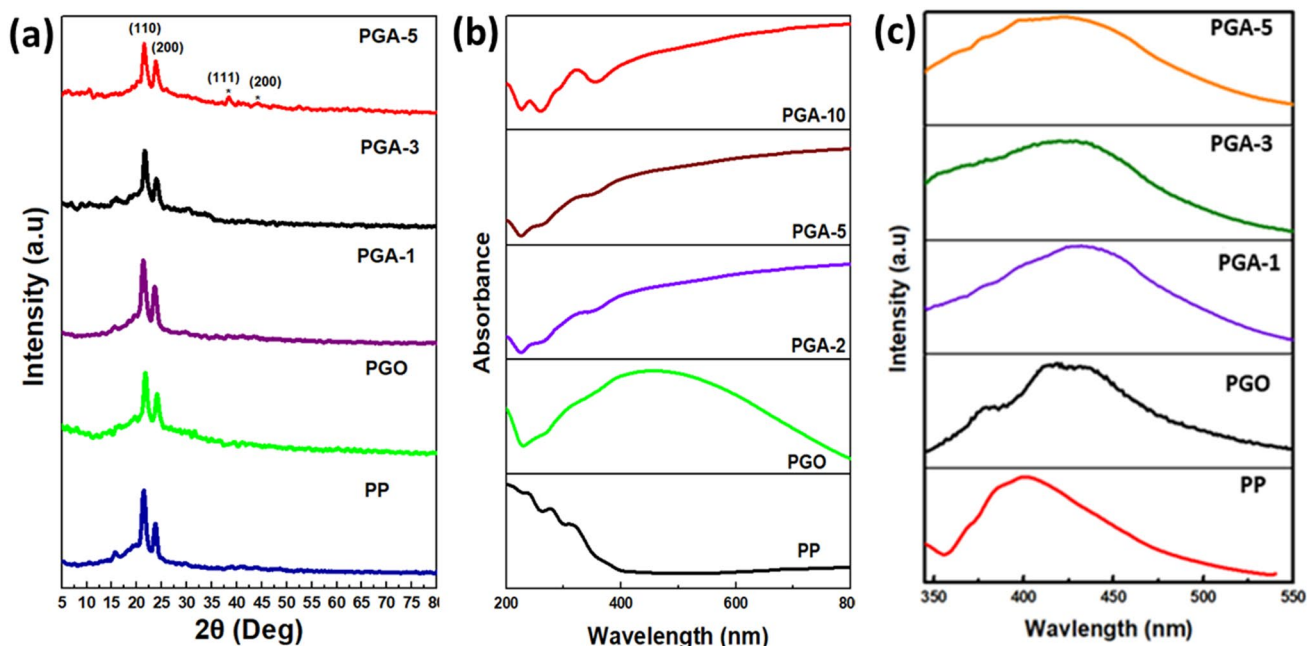
Fig. 8 **a** The XRD profiles of the pure PCL and nanoparticle incorporated PCL films: PP- pure PCL, PGO–PCL film comprising of GO, PGA-1—PCL film with Ag–GO nanohybrid (1 wt% Ag), PGA-3—PCL film with Ag–GO nanohybrid (3 wt% Ag), PGA-5—PCL film with Ag–GO nanohybrid (5 wt% Ag). **b** UV–Vis absorption spectra of the casted polymer films – PP- pure PCL, PGO–PCL film compris-ing of GO, PGA-1—PCL film with Ag–GO nanohybrid (1 wt% Ag), PGA-3—PCL film with Ag–GO nanohybrid (3 wt% Ag), PGA-5—PCL film with Ag–GO nanohybrid (5 wt% Ag). **c** Photoluminescence emission spectra of PCL films incorporated with GO, GO–1Ag, GO–3Ag, and GO–5Ag nanofillers

3.2.4 Photoluminescence

The PL spectra of various samples viz., PP, PGO, PGA-1, PGA-3 and PGA-5, are shown in Fig. 8c. On excitation at 410 nm, the PL spectra showed broad bands at 399 nm, 421 nm, 428 nm, 427 nm ,423 nm for PP, PGO, PGA-1, PGA-3 and PGA-5, respectively. This result is strikingly different from that obtained for the nanoparticle systems. Thus, the emission property is influenced by the polymer and it contributes to the broad emission. In addition, only one broad band is observed for Ag–GO incorporated polymer samples. In the case of PP, the band is centred at 400 nm while PGO shows two bands at 378 and 421 nm. These distinct bands are not observed for the Ag–GO nanoparticles incorporated in the polymer matrix. Therefore, it is inferred that the emission bands arise from excited states that are close in energy, contributed by Ag, GO and PCL.

3.2.5 Water Contact Angle

The variation of hydrophobic nature of pure PCL with that of the hybrid polymer nanocomposites was estimated through the water contact angle analysis as shown in Fig. 9a. Water contact angle around 76.4° for pure PCL, validates its notable hydrophobic nature. A diminution in the angle measurement to 73.8° was noticed for PCL-GO nanocomposite,

following the inclusion of GO nanoparticles. The introduction of Ag–GO nanohybrid, with varying AgNP concentrations (1%, 3% and 5%), into the PCL matrix showed a considerable reduction in its hydrophobicity with values 70.1°, 64.8° and 56° for PCL-GO–Ag (1%), PCL-GO–Ag (3%) and PCL-GO–Ag (5%) respectively. In a work done by Kumar et al., the nanocomposite composed of PCL and GO displayed an improved surface wettability with a contact angle of 77° than that of the PCL/rGO nanocomposite, which authenticates the vital role of GO in PCL matrix for enriched bioactivity [56]. Also, in a similar work on PCL/rGO–Ag nanocomposite system by Kumar et al., a notable hydrophilic behaviour was depicted by the prepared nanocomposite with a contact angle of 79.2°, in comparison with that of the pure PCL [51]. An essential relationship exists between the biological behaviour of a particular nanomaterial and its extent of surface wettability. Biomaterials with hydrophilic nature accelerate the process of cell adhesion and its proliferation [85, 86]. Thus, functionalization of polymers that are hydrophobic, for example PCL, is normally done in order to enhance its surface wettability [85]. Incorporation of nanoparticles like GO and Ag into PCL, drastically improvised its wettability nature. Therefore, by incorporating the hydrophilic nanohybrids into the polymer intensify its surface wettability [41].
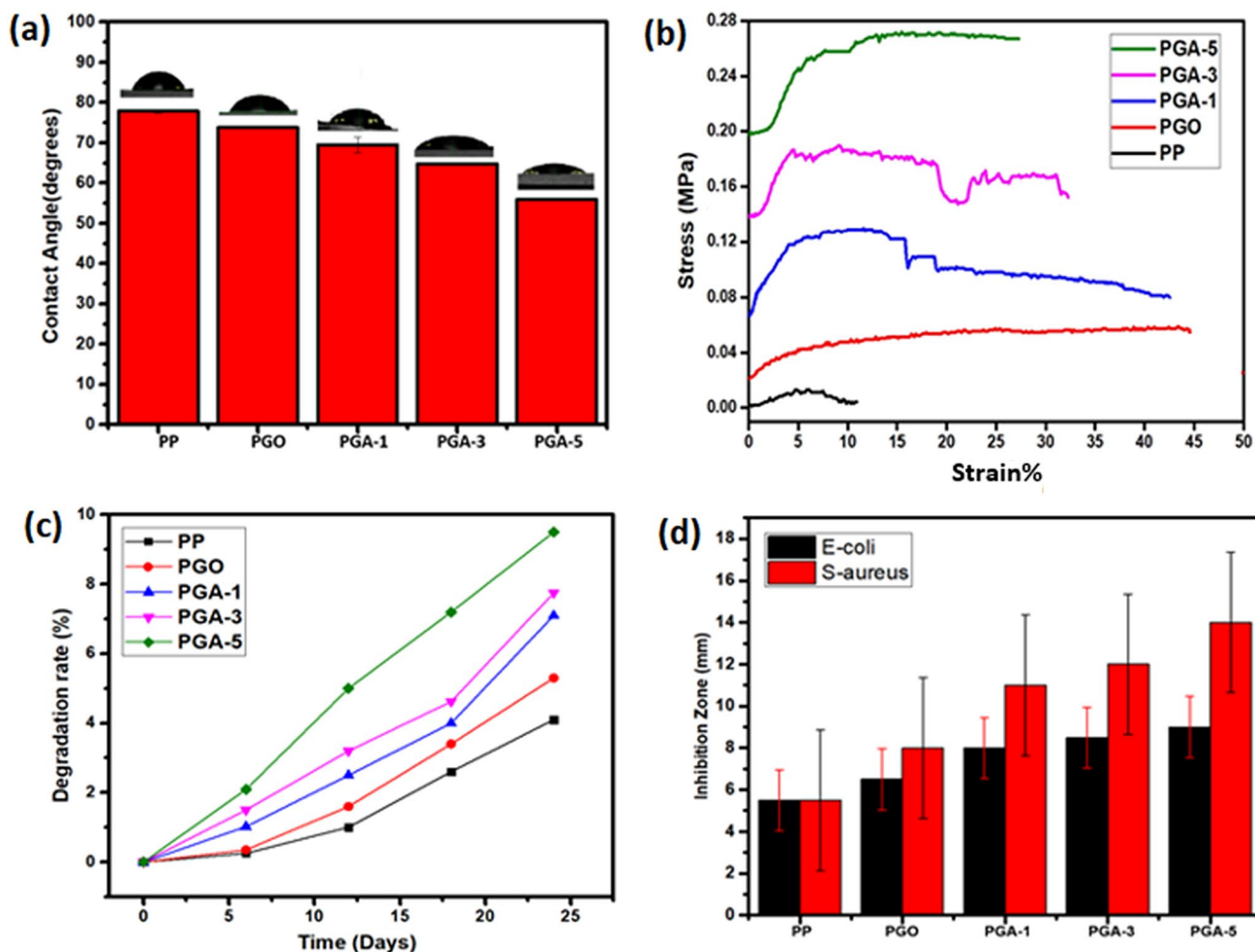
Fig. 9 **a** Water contact angle measurements of pure and nanoparticle incorporated PCL films by Sessile drop method. **b** The stress-strain curve of the prepared PCL, PCL/GO, PCL/GO–Ag (1 wt%), PCL/GO–Ag (3 wt%), and PCL/GO–Ag (5 wt%) films. **c** The rate of biodegradation of as-synthesized polymer films - PCL, PCL/GO, PCL/

GO–Ag (1 wt%), PCL/GO–Ag (3 wt%), and PCL/GO–Ag (5 wt%) – in PBS solution. **d** Antibacterial behaviour of PCL, PCL/GO, PCL/GO–Ag (1 wt%), PCL/GO–Ag (3 wt%), and PCL/GO–Ag (5 wt%) films against *E. coli* and *S. aureus*

3.2.6 Mechanical Behaviour of PCL Nanocomposites

Various mechanical attributes of pure PCL and the nanoparticle incorporated composites are enlisted in Table 2 and its corresponding stress-strain plot is given in Fig. 9b. Pure PCL film displayed tensile strength of 9.2 MPa and a corresponding Young's Modulus value of 1.5 MPa. The incorporation of GO as nanofillers into the PCL matrix slightly improved the tensile strength and Young's modulus to 11.8 MPa and 2.8 MPa, respectively. It was seen that as the concentration of AgNPs in the nanocomposites is increasing, the tensile strength is also considerably enhanced upto 41.6 MPa with an appealing Young's modulus of 38.8 MPa. The Ag–GO nanohybrid was found to be more efficient in boosting the mechanical attributes of PCL. Uniform dispersivity and ameliorated surface interactions of graphene in

Table 2 Mechanical attributes of PCL, PCL/GO, PCL/GO–Ag (1 wt%), PCL/GO–Ag (3 wt%) and PCL/GO–Ag (5 wt%)

Sample code	Tensile strength (MPa)	Young's modulus (MPa)
PP	9.2	1.5
PGO	11.8	2.8
PGA-1	19.9	4.3
PGA-3	21.6	63.7
PGA-5	41.6	38.8

PCL, convincingly strengthens the PCL nanocomposites and also shows improved load transfer from PCL to the nanofiller [87]. The visible growth in the mechanical behaviours of PCL/GO–Ag nanocomposites could be credited to the

even dispersion of nanofillers in the polymer. Due to high exfoliation of Ag–GO when compared to that of the GO sheets, PCL/GO–Ag showed better mechanical properties than PCL/GO. It is seen that the mechanical attributes of a polymer matrix is highly influenced by the dispersivity of the nanofiller [88]. In addition to it, the stacking of GO sheets could be prevented by decorating AgNPs over GO, which leads to highly exfoliated Ag–GO dispersion in the PCL nanocomposite. Prior studies also substantiated that the metallic nanoparticle adornment over the GO sheet, reduced the graphene sheet restacking, and thus hindered its aggregation [65]. For instance, Jaidev et al. have shown that anchoring of CuNPs over graphene sheets prevented graphene layer restacking as well as reduced the agglomeration of nanoparticles, which facilitated the homogenous dispersivity of graphene flakes in the polymeric system, followed by better load transfer [89]. Therefore, from the obtained data, it can be concluded that anchoring AgNPs over GO surface could improve the mechanical characteristics of PCL, as a result of an excellent dispersivity in the polymer.

3.2.7 Biodegradation Studies

The degradation rate and the bioresorbability of PCL frame is notably affected when nanofillers are incorporated into it. Biodegradation rates of pure and nanoparticle incorporated PCL films in phosphate buffer saline (PBS) are shown in Fig. 9c. Pure polymer film (PP) displayed a slower rate of degradation where 1% weight reduction was seen on day 12. This could be ascribed towards the hydrophobicity of pure PCL. In addition, PCL/GO and PCL/GO–Ag nanocomposite exhibited a comparatively quicker degradation rate because of the existence of hydrophilic nanohybrid, which is clearly validated by the surface wettability studies as detailed earlier. Seyedsalehi et al. demonstrated that the incorporation of rGO into the PCL matrix enhanced the rate of degradation from 0.75 to 1.25% in 14 days [90]. In our work, the presence of enormous hydrophilic functional moieties on GO surface than rGO, augments the hydrophilic nature of the PCL matrix, which could hydrate the polymer and promote its water uptaking nature, thus resulting in swift biodegradation [91]. Furthermore, the silver ion release from the nanocomposites create voids, which act as suitable sites to be occupied by water molecules. In the same manner, Kumar et al. substantiated that the strontium ion release from the fabricated PCL/rGO/Sr nanocomposite eased its rate of degradation [41].

3.2.8 Antibacterial Studies

The antibacterial activities of the polymer nanocomposites against the gram positive (*S. aureus*) and gram negative (*E. coli*) bacteria were investigated (Fig. 9d). The procured

results point out the enhanced antibacterial effect of Ag incorporated polymer scaffolds in comparison to pure PCL. The noticed inhibition zone by the PCL/GO film could be ascribed to the antibacterial property of graphene-based nanomaterials either from the creation of oxidative stress or by puncturing the membrane of the bacterial cells [44]. The two-dimensional planar GO structure enabled it to serve as nano-knives and pierce the bacterial cell wall, which ultimately causes its destruction. The bacterial cell wall system influences GO nanosheets to interact differently with *E. coli* and *S. aureus*, i.e. the presence of additional layer in gram negative bacteria (*E. coli*), contrary to gram positive bacteria (*S. aureus*), decelerate the perforation rate of the GO sheets through the bacterial cell wall [92]. The incorporation of silver decorated GO into the polymer matrix significantly enhanced the antibacterial efficiency, which accredited to the combined upshot of both GO and silver nanoparticles. For Ag decorated GO nanohybrid, the considerable surface area of GO provide Ag^+ ion release and effectively support the bacterial cell interaction with the anchored AgNPs [93]. The released Ag^+ ions then firmly attaches with the thiol groups of the proteins and enzymes present on the bacterial cell surface, which may inhibit their replication and give onto their death [94]. The production of ROS by the silver nanoparticles can create oxidative stress, damage the proteins and enzymes, and finally cause irreparable disruption to the process of replication of DNA [95]. In addition, nanoparticles with antibacterial property when affixed over the GO frame, is found to be highly stable and effectively dispersed. Pure AgNPs tend to agglomerate when they interact with the bacterial membrane, which give rise to reduced vital surface area and thus, diminished antibacterial effect [96, 97]. In a similar work by Reza et al., incorporation of GO/Ag nanohybrid into PLLA polymeric system, efficaciously improvised the antibacterial performance of the nanocomposite against both *E. coli* and *S. aureus* [98]. Therefore, in our work, AgNPs have been introduced onto GO substrate to effectually get rid of such limitations.

3.2.9 Biomineralization

Figure 10 depict the SEM micrographs and EDAX spectra of the PCL nanocomposites after 15 days of immersion in SBF, at room temperature. In PCL/GO–Ag film (Fig. 10f), a compact formation of aggregates was found over its surface when compared to pure and GO incorporated PCL films (Fig. 10d, e), which indicates that the addition of GO and Ag–GO effectuates the alteration of the surface behaviour of pure polymer. That is, the occurrence of anionic moieties in GO and Ag–GO promote the deposition of Ca^{2+} cations over the polymer nanocomposite and thus induces biomineralization. Additionally, it is clearly evident from the obtained spectra that PCL/GO–Ag film (Fig. 10c)

encourages biomineralization over its surface with a Ca/P ratio of 1.5, when compared to that of pure and GO incorporated PCL films (Fig. 10a, b), which validates the formation of apatite.

So, the results obtained throughout our work validate that incorporating Ag–GO nanohybrid into polymer frame provides a versatile nanocomposite in contrast with PCL and PCL/GO films. Ag–GO nanohybrid act as an effectual nanofiller for making a better nanocomposite with luminescence, better hydrophilicity, improved mechanical strength, high antibacterial property and effectual bioactivity. These biodegradable polymer complexes are envisioned for utilization in bio-applications like bioimaging, synthetic bone grafts and ecological food packing materials.

4 Conclusions

In summary, an easy and effective route to synthesize a nanohybrid that encompass GO nanosheets and metallic AgNPs was established. The physicochemical and optical behaviours of the as-synthesized nanoparticles were comprehensively evaluated by various characterization methods such as XRD, SEM-EDAX, TEM, FTIR, XPS, Raman analysis, UV–Vis spectroscopy and PL. The SEM and TEM micrographs establish the efficacious adhesion of spherical AgNPs over the GO sheet surface and the corresponding EDAX spectra attest the same. The pure crystalline AgNPs over graphene surface were detected in the XRD pattern and the anchored functional groups in the nanoparticles were analysed from the FTIR spectrum. The intensification in the Raman spectrum for Ag–GO, evinces the SERS activity offered by the AgNPs over the GO sheet surface. In addition, the chemical state and composition of the as-prepared Ag–GO nanohybrid was analysed by the XPS technique. The increment in the luminescence peak intensity of Ag decorated GO owes to the combined effect of surface plasmon resonance (LSPR) of Ag nanoparticles and the intrinsic luminescence of GO. Finally, the as-synthesized nanoparticles were incorporated into PCL matrix and were casted into polymeric films. Further characterizations on these nanocomposites showed that they enabled enhanced exfoliation and better dispersion of GO and Ag–GO in the polymer frame. Even dispersion of Ag–GO nanohybrid in the PCL matrix augmented its surface wettability and mechanical strength. The combined effect of GO and Ag nanoparticles in the polymer film significantly improvised its antibacterial effect against *E. coli* and *S. aureus*. Furthermore, a notable degradation rate was observed for PCL/GO–Ag nanocomposites with improved biomineralization. Thus, Ag–GO nanohybrid perform as a potent nanofiller for fabricating a suitable nanocomposite with luminescence, better hydrophilicity, improved mechanical strength, high antibacterial property
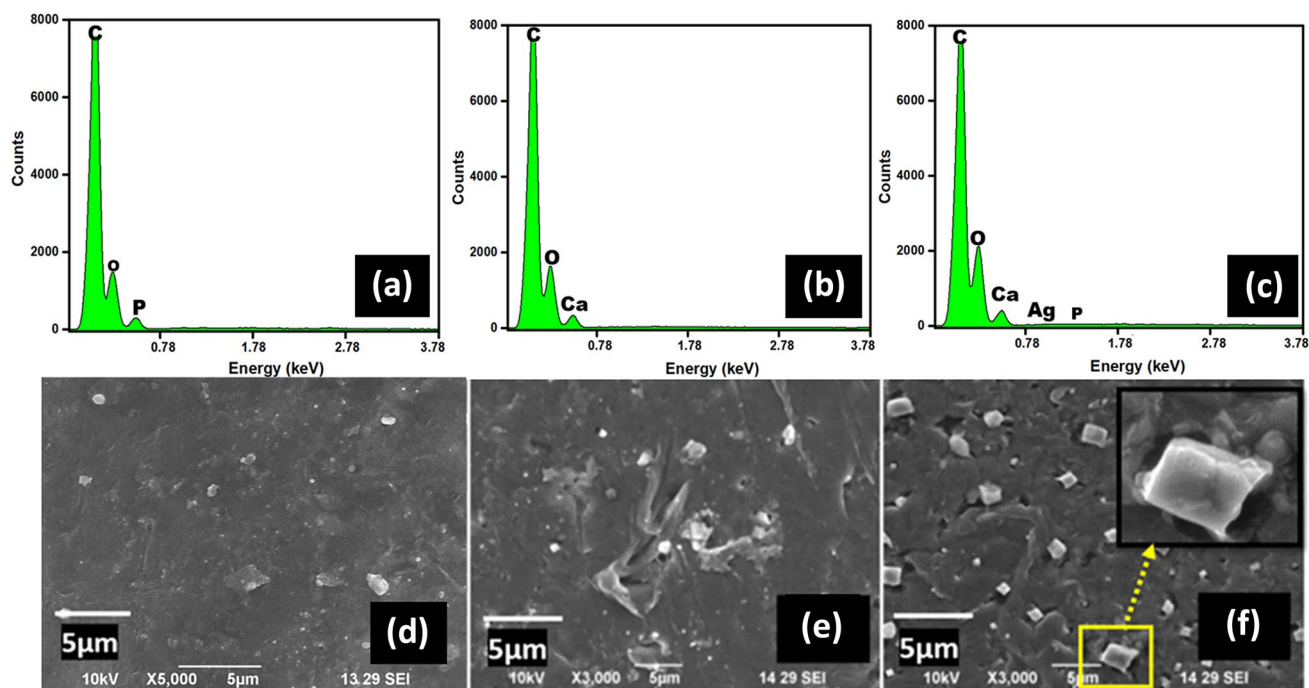

Fig. 10 EDAX spectra of **a** pure PCL, **b** GO incorporated PCL, **c** Ag–GO incorporated PCL after 15 days biomineralization activity using simulated body fluid (SBF) solution and the corresponding apatite formation is depicted in the SEM micrographs of **d** pure PCL, **e** GO incorporated PCL, **f** Ag–GO (inset- the magnified image of apatite formation)

and effectual bioactivity. Therefore, the obtained nano-composite films act as a biodegradable multifunctional agent with conceivable applications comprising of bioimaging, scaffolds for tissue engineering and bioresorbable bone repairing devices.

Data Availability All data generated or analysed during this study are included in this published article.

Declarations

Conflict of interest The authors declare that there is no competing financial interest.

References

1. S. Yang, K.F. Leong, Z. Du, C.K. Chua, The design of scaffolds for use in tissue engineering. Part I. Traditional factors. Tissue Eng. **7**(6), 679–689 (2004). https://doi.org/10.1089/1076327017 53337645

2. J. Sharma, M. Lizu, M. Stewart, K. Zygula, Y. Lu, R. Chauhan, X. Yan, Z. Guo, E. Wujcik, S. Wei, Multifunctional nanofibers towards active biomedical therapeutics. Polymers **7**(2), 186–219 (2015). https://doi.org/10.3390/polym7020186

3. M. Barani, M. Mukhtar, A. Rahdar, S. Sargazi, S. Pandey, M. Kang, Recent advances in nanotechnology-based diagnosis and treatments of human osteosarcoma. Biosensors **11**(2), 55 (2021). https://doi.org/10.3390/BIOS11020055

4. A. Rauf, T.A. Tabish, I.M. Ibrahim, M. Rauf ul Hassan, S. Tahseen, M. Abdullah Sandhu, G. Shahnaz, A. Rahdar, M. Cucchiarini, S. Pandey, Design of mannose-coated rifampicin nanoparticles modulating the immune response and rifampicin induced hepatotoxicity with improved oral drug delivery. Arab. J. Chem. **14**(9), 103321 (2021). https://doi.org/10.1016/j.arabjc.2021. 103321

5. A. Rahdar, M.R. Hajinezhad, M. Barani, S. Sargazi, M. Zaboli, E. Ghazy, F. Baino, M. Cucchiarini, M. Bilal, S. Pandey, Pluronic F127/doxorubicin microemulsions: preparation, characterization, and toxicity evaluations. J. Mol. Liq. (2021). https://doi.org/10. 1016/j.molliq.2021.117028

6. D. Ozdil, H.M. Aydin, Polymers for medical and tissue engineering applications. J. Chem. Technol. Biotechnol. **89**(12), 1793–1810 (2014). https://doi.org/10.1002/jctb.4505

7. R. Eivazzadeh-Keihan, E. Bahojb Noruzi, K. Khanmohammadi Chenab, A. Jafari, F. Radinekiyan, S.M. Hashemi, F. Ahmadpour, A. Behboudi, J. Mosafer, A. Mokhtarzadeh, A. Maleki, M.R. Hamblin, Metal-based nanoparticles for bone tissue engineering. J. Tissue Eng. Regen. Med. **14**(12), 1687–1714 (2020). https:// doi.org/10.1002/term.3131

8. S. Zinatloo-Ajabshir, M.S. Morassaei, O. Amiri, M. Salavati-Niasari, L.K. Foong, Nd2Sn2O7 nanostructures: green synthesis

9. and characterization using date palm extract, a potential electrochemical hydrogen storage material. Ceram. Int. **46**(11), Part A, 17186–17196 (2020). https://doi.org/10.1016/j.ceramint.2020.03. 014

9. S. Moshtaghi, S. Zinatloo-Ajabshir, M. Salavati-Niasari, Nanocrystalline barium stannate: facile morphology-controlled preparation, characterization and investigation of optical and photocatalytic properties. J. Mater. Sci.: Mater. Electron. **27**, 834–842 (2016). https://doi.org/10.1007/s10854-015-3824-3

10. M. Mousavi-Kamazani, S. Zinatloo-Ajabshir, M. Ghodrati, One-step sonochemical synthesis of Zn(OH)2/ZnV3O8 nanostructures as a potent material in electrochemical hydrogen storage. J. Mater. Sci.: Mater. Electron. **31**, 17332–17338 (2020). https://doi.org/10. 1007/s10854-020-04289-4

11. S. Zinatloo-Ajabshir, S.A. Heidari-Asil, M. Salavati-Niasari, Recyclable magnetic ZnCo2O4-based ceramic nanostructure materials fabricated by simple sonochemical route for effective sunlight-driven photocatalytic degradation of organic pollution. Ceram. Int. **47**(7), Part A, 8959–8972 (2021). https://doi.org/10. 1016/j.ceramint.2020.12.018

12. S. Zinatloo-Ajabshir, M.S. Morassaei, M. Salavati-Niasari, Eco-friendly synthesis of Nd 2 Sn 2 O 7 –based nanostructure materials using grape juice as green fuel as photocatalyst for the degradation of erythrosine. Compos. B: Eng. **167**, 643–653 (2019). https://doi.org/10.1016/j.compositesb.2019.03.045

13. S. Zinatloo-Ajabshir, M. Baladi, M. Salavati-Niasari, Sono-synthesis of MnWO4 ceramic nanomaterials as highly efficient photocatalysts for the decomposition of toxic pollutants. Ceram. Int. **47**(21), 30178–30187 (2021). https://doi.org/10.1016/j.ceram int.2021.07.197

14. S. Zinatloo-Ajabshir, S.A. Heidari-Asil, M. Salavati-Niasari, Simple and eco-friendly synthesis of recoverable zinc cobalt oxide-based ceramic nanostructure as high-performance photocatalyst for enhanced photocatalytic removal of organic contamination under solar light. Sep. Purif. Technol. **267**, 118667 (2021). https:// doi.org/10.1016/j.seppur.2021.118667

15. S. Zinatloo-Ajabshir, M. Mousavi-Kamazani, Recent advances in nanostructured Sn–Ln mixed-metal oxides as sunlight-activated nanophotocatalyst for high-efficient removal of environmental pollutants. Ceram. Int. **47**(17), 23702–23724 (2021). https://doi.org/ 10.1016/j.ceramint.2021.05.155

16. H. Etemadi, S. Afsharkia, S. Zinatloo-Ajabshir, E. Shokri, Effect of alumina nanoparticles on the antifouling properties of poly-carbonate-polyurethane blend ultrafiltration membrane for water treatment. Polym. Eng. Sci. **61**(9), 2364–2375 (2021). https://doi. org/10.1002/pen.25764

17. H. Safajou, M. Ghanbari, O. Amiri, H. Khojasteh, F. Namvar, S. Zinatloo-Ajabshir, M. Salavati-Niasari, Green synthesis and characterization of RGO/Cu nanocomposites as photocatalytic degradation of organic pollutants in waste-water. Int. J. Hydrog. Energy **46**(39), 20534–20546 (2021). https://doi.org/10.1016/j. ijhydene.2021.03.175

18. S. Zinatloo-Ajabshir, M. Baladi, M. Salavati-Niasari, Enhanced visible-light-driven photocatalytic performance for degradation of organic contaminants using PbWO4 nanostructure fabricated by a new, simple and green sonochemical approach. Ultrason. Sonochem. **72**, 105420 (2021). https://doi.org/10.1016/j.ultsonch. 2020.105420

19. S. Sarkar, E. Guibal, F. Quignard, A.K. SenGupta, Polymer-supported metals and metal oxide nanoparticles: Synthesis, characterization, and applications. J. Nanopart. Res. **14**, 715 (2012). https://doi.org/10.1007/s11051-011-0715-2

20. F. Mohandes, M. Salavati-Niasari, In vitro comparative study of pure hydroxyapatite nanorods and novel polyethylene glycol/graphene oxide/hydroxyapatite nanocomposite. J. Nanopart. Res. **16**, 2604 (2014). https://doi.org/10.1007/s11051-014-2604-y

21. L. Li, K. Xia, L. Li, S. Shang, Q. Guo, G. Yan, Fabrication and characterization of free-standing polypyrrole/graphene oxide nanocomposite paper. J. Nanopart. Res. **14**, 908 (2012). https://doi.org/10.1007/s11051-012-0908-3

22. D. Nuvoli, V. Alzari, R. Sanna, S. Scognamillo, J. Alongi, G. Malucelli, A. Mariani, Synthesis and characterization of graphene-based nanocomposites with potential use for biomedical applications. J. Nanopart. Res. **15**, 1515 (2013). https://doi.org/10.1007/s11051-013-1512-x

23. M. Alazzawi, N.A. Alsahib, H.T. Sasmazel: Optimization of electrospinning parameters for poly (vinyl alcohol) and glycine electrospun nanofibers. EasyChair (2021). https://easychair.org/publications/preprint/xxF5

24. A.O. Basar, S. Castro, J.M. Lagaron, H.T. Sasmazel, Novel poly(ε-caprolactone)/gelatin wound dressings prepared by emulsion electrospinning with controlled release capacity of Ketoprofen anti-inflammatory drug. Mater. Sci. Eng. C: Mater. Biol. Appl. **81**, 459–468 (2017). https://doi.org/10.1016/j.msec.2017.08.025

25. K. Zhou, R. Gao, S. Jiang, Morphology, thermal and mechanical properties of poly (ε-caprolactone) biocomposites reinforced with nano-hydroxyapatite decorated graphene. J. Colloid Interface Sci. **496**, 334–342 (2017). https://doi.org/10.1016/j.jcis.2017.02.038

26. R. Scaffaro, F. Lopresti, A. Maio, L. Botta, S. Rigogliuso, G. Ghersi, P.C.L. Electrospun, GO-g-PEG structures: processing-morphology- properties relationships. Compos. A: Appl. Sci. Manuf. **92**, 97–107 (2017). https://doi.org/10.1016/j.compositesa.2016.11.005

27. A. Behboudi, Y. Jafarzadeh, R. Yegani, Polyvinyl chloride/polycarbonate blend ultrafiltration membranes for water treatment. J. Membr. Sci. **534**, 18–24 (2017). https://doi.org/10.1016/j.memsci.2017.04.011

28. N. Guan, P. Chew, S. Zhao, C. Malde, R. Wang, Superoleophobic surface modification for robust membrane distillation performance. J. Membr. Sci. **541**, 162–173 (2017). https://doi.org/10.1016/j.memsci.2017.06.089

29. Y. Liu, L. Li, N. Pan, Y. Wang, X. Ren, Antibacterial cellulose acetate films incorporated with N-halamine-modified nano-crystalline cellulose particles. Polym. Adv. Technol. **28**(4), 463–469 (2016). https://doi.org/10.1002/pat.3906

30. R. Nirmala, H. Kang, H. Park, R. Navamathavan, I.S. Jeong, H.Y. Kim, Silver-loaded biomimetic hydroxyapatite grafted poly(ε-caprolactone) composite nanofibers: A cytotoxicity study. J. Biomed. Nanotechnol. **8**(1), 125–132 (2012). https://doi.org/10.1166/jbn.2012.1359

31. R. Nirmala, K. Taek, D. Kwang, B. Woo-il, R. Navamathavan, H. Yong, Structural, thermal, mechanical and bioactivity evaluation of silver-loaded bovine bone hydroxyapatite grafted poly(ε-caprolactone) nanofibers via electrospinning. Surf. Coat. Technol. **205**(1), 174–181 (2010). https://doi.org/10.1016/j.surfcoat.2010.06.027

32. R. De Santis, A. Russo, A. Gloria, U. D'Amora, T. Russo, S. Panseri, M. Sandri, A. Tampieri, M. Marcacci, V.A. Dediu, C.J. Wilde, L. Ambrosio, Towards the design of 3D fiber-deposited poly(ε-caprolactone)/Iron-doped hydroxyapatite nanocomposite magnetic scaffolds for bone regeneration. J. Biomed. Nanotechnol. **11**(7), 1236–1246 (2015). https://doi.org/10.1166/jbn.2015.2065

33. K. Turcheniuk, R. Boukherroub, S. Szunerits, Gold–graphene nanocomposites for sensing and biomedical applications. J. Mater. Chem. B. **3**(21), 4301–4324 (2015). https://doi.org/10.1039/C5TB00511F

34. P.K. Sandhya, J. Jose, M.S. Sreekala, M. Padmanabhan, N. Kalarikkal, S. Thomas, Reduced graphene oxide and ZnO decorated graphene for biomedical applications. Ceram. Int. **44**(13), 15092–15098 (2018). https://doi.org/10.1016/j.ceramint.2018.05.143

35. C. Liu, J. Shen, K.W.K. Yeung, S.C. Tjong, Development and antibacterial performance of novel polylactic acid-graphene oxide-silver nanoparticle hybrid nanocomposite mats prepared by electrospinning. ACS Biomater. Sci. Eng. **3**(3), 471–486 (2017). https://doi.org/10.1021/acsbiomaterials.6b00766

36. A.K. Geim, Graphene: status and prospects. Science **324**(5934), 1530–1534 (2009). https://doi.org/10.1126/science.1158877

37. A. Kumar, K.M. Rao, S.S. Han, Mechanically viscoelastic nanoreinforced hybrid hydrogels composed of polyacrylamide, sodium carboxymethylcellulose, graphene oxide, and cellulose nanocrystals. Carbohydr. Polym. **193**, 228–238 (2018). https://doi.org/10.1016/j.carbpol.2018.04.004

38. A. Kumar, S.M. Zo, J.H. Kim, S.C. Kim, S.S. Han, Enhanced physical, mechanical, and cytocompatibility behavior of polyelectrolyte complex hydrogels by reinforcing halloysite nanotubes and graphene oxide. Compos. Sci. Technol. **175**, 35–45 (2019). https://doi.org/10.1016/j.compscitech.2019.03.008

39. Y. Li, C. Liu, H. Zhai, G. Zhu, H. Pan, X. Xu, R. Tang, Biomimetic graphene oxide-hydroxyapatite composites via in situ mineralization and hierarchical assembly. RSC Adv. **4**(48), 25398–25403 (2014). https://doi.org/10.1039/c4ra02821j

40. Y. Li, T. Yu, T. Yang, L. Zheng, K. Liao, Bio-inspired nacre-like composite films based on graphene with superior mechanical, electrical, and biocompatible properties. Adv. Mater. **24**(25), 3426–3431 (2012). https://doi.org/10.1002/adma.201200452

41. S. Kumar, K. Chatterjee, Strontium eluting graphene hybrid nanoparticles augment osteogenesis in a 3D tissue scaffold. Nanoscale **7**(5), 2023–2033 (2015). https://doi.org/10.1039/c4nr05060f

42. X. Zou, L. Zhang, Z. Wang, Y. Luo, X. Zou, L. Zhang, Z. Wang, Y. Luo, Mechanisms of the antimicrobial activities of graphene materials. J. Am. Chem. Soc. **138**(7), 2064–2077 (2016). https://doi.org/10.1021/jacs.5b11411

43. S. Liu, T.H. Zeng, M. Hofmann, E. Burcombe, J. Wei, R. Jiang, J. Kong, Y. Chen, Antibacterial activity of graphite, graphite oxide, graphene oxide, and reduced graphene oxide: membrane and oxidative stress. ACS Nano **5**(9), 6971–6980 (2011). https://doi.org/10.1021/nn202451x

44. N. Pan, Y. Liu, X. Fan, Z. Jiang, X. Ren, J. Liang, Preparation and characterization of antibacterial graphene oxide functionalized with polymeric N-halamine. J. Mater. Sci. **52**, 1996–2006 (2017). https://doi.org/10.1007/s10853-016-0488-1

45. S. Shahmoradi, H. Golzar, M. Hashemi, V. Mansouri, M. Omidi, F. Yazdian, A. Yadegari, L. Tayebi, Optimizing the nanostructure of graphene oxide/silver/arginine for effective wound healing. Nanotechnology **29**(47), 475101 (2018). https://doi.org/10.1088/1361-6528/aadedc

46. R. Dastjerdi, M. Montazer, A review on the application of inorganic nano-structured materials in the modification of textiles: focus on anti-microbial properties. Colloids Surf. B Biointerfaces **79**(1), 5–18 (2010). https://doi.org/10.1016/j.colsurfb.2010.03.029

47. L. Balogh, D.R. Swanson, D.A. Tomalia, G.L. Hagnauer, A.T. McManus, Dendrimer-silver complexes and nanocomposites as antimicrobial agents. Nano Lett. **1**(1), 18–21 (2001). https://doi.org/10.1021/nl005502p

48. M. Hassanisaadi, G.H.S. Bonjar, A. Rahdar, S. Pandey, A. Hosseinipour, R. Abdolshahi, Environmentally safe biosynthesis of gold nanoparticles using plant water extracts. Nanomater **11**(8), 2033 (2021). https://doi.org/10.3390/NANO11082033

49. M. Barani, S.M. Hosseinikhah, A. Rahdar, L. Farhoudi, R. Arshad, M. Cucchiarini, S. Pandey, Nanotechnology in bladder cancer: diagnosis and treatment. Cancers **13**(9), 2214 (2021). https://doi.org/10.3390/CANCERS13092214

50. G. Das, H.S. Shin, A. Kumar, C.N. Vishnuprasad, J.K. Patra, Photo-mediated optimized synthesis of silver nanoparticles using the extracts of outer shell fibre of *Cocos nucifera* L. fruit and

detection of its antioxidant, cytotoxicity and antibacterial potential. Saudi. J. Biol. Sci. **28**(1), 980–987 (2021). https://doi.org/10.1016/j.sjbs.2020.11.022

51. S. Kumar, S. Raj, S. Jain, K. Chatterjee, Multifunctional biodegradable polymer nanocomposite incorporating graphene-silver hybrid for biomedical applications. Mater. Des. **108**, 319–332 (2016). https://doi.org/10.1016/j.matdes.2016.06.107

52. W. Shao, X. Liu, H. Min, G. Dong, Q. Feng, S. Zuo, Preparation, characterization, and antibacterial activity of silver nanoparticle-decorated graphene oxide nanocomposite. ACS Appl. Mater. Interfaces. **7**(12), 6966–6973 (2015). https://doi.org/10.1021/acsami.5b00937

53. J. Mohammadnejad, F. Yazdian, M. Omidi, A.D. Rostami, B. Rasekh, A. Fathinia, Graphene oxide/silver nanohybrid: optimization, antibacterial activity and its impregnation on bacterial cellulose as a potential wound dressing based on GO-Ag nanocomposite-coated BC. Eng. Life Sci. **18**, 298–307 (2018). https://doi.org/10.1002/elsc.201700138

54. S. Shahmoradi, H. Golzar, M. Hashemi, V. Mansouri, M. Omidi, F. Yazdian, A. Yadegari, L. Tayebi, Optimizing the nanostructure of graphene oxide/silver/arginine for effective wound healing. Nanotechnology. **29**(47), 475101 (2018). https://doi.org/10.1088/1361-6528/aadedc

55. N. Pan, Y. Wei, M. Zuo, R. Li, X. Ren, T.S. Huang, Antibacterial poly (ε-caprolactone) fibrous membranes filled with reduced graphene oxide-silver. Colloids Surf. A: Physicochem. Eng. Asp. **603**, 125186 (2020). https://doi.org/10.1016/j.colsurfa.2020.125186

56. S. Kumar, D. Azam, S. Raj, E. Kolanthai, K.S. Vasu, A.K. Sood, K. Chatterjee, 3D scaffold alters cellular response to graphene in a polymer composite for orthopedic applications. J. Biomed. Mater. Res. B: Appl. Biomater. **104**(4), 732–749 (2016). https://doi.org/10.1002/jbm.b.33549

57. W.S. Hummers, R.E. Offeman, Preparation of graphitic oxide. J. Am. Chem. Soc. **80**(6), 1339 (1958). https://doi.org/10.1021/ja01539a017

58. S. Kumari, P. Sharma, S. Yadav, J. Kumar, A. Vij, P. Rawat, S. Kumar, C. Sinha, J. Bhattacharya, C.M. Srivastava, S. Majumder, A novel synthesis of the graphene oxide-silver (GO-Ag) nanocomposite for unique physiochemical applications. ACS Omega **5**(10), 5041–5047 (2020). https://doi.org/10.1021/acsomega.9b03976

59. W.K. Chee, H.N. Lim, N.M. Huang, I. Harrison, Nanocomposites of graphene/polymers: a review. RSC Adv. **5**(83), 68014–68051 (2015). https://doi.org/10.1039/c5ra07989f

60. F. Han Lyn, C. Peng, T. Ruzniza, M.Z. Nur Hanani, Effect of oxidation degrees of graphene oxide (GO) on the structure and physical properties of chitosan/GO composite films. Food Packag. Shelf Life **21**, 100373 (2019). https://doi.org/10.1016/j.fpsl.2019.100373

61. K.R. Xiong, Y.R. Liang, Y. Ou-Yang, D.C. Wu, R.W. Fu, Nanohybrids of silver nanoparticles grown in-situ on a graphene oxide silver ion salt: simple synthesis and their enhanced antibacterial activity. Xinxing Tan Cailiao/New Carbon Mater. **34**(5), 426–433 (2019). https://doi.org/10.1016/S1872-5805(19)60024-7

62. W. Yuan, Y. Gu, L. Li, Green synthesis of graphene/Ag nanocomposites. Appl. Surf. Sci. **261**, 753–758 (2012). https://doi.org/10.1016/j.apsusc.2012.08.094

63. X. Zhang, H. Sun, S. Tan, J. Gao, Y. Fu, Z. Liu, Hydrothermal synthesis of Ag nanoparticles on the nanocellulose and their antibacterial study. Inorg. Chem. Commun. **100**, 44–50 (2019). https://doi.org/10.1016/j.inoche.2018.12.012

64. M. Cobos, I. De-La-pinta, G. Quindós, M.D. Fernández, M.J. Fernández, Graphene oxide–silver nanoparticle nanohybrids: Synthesis, characterization, and antimicrobial properties. Nanomaterials. **10**(2), 376 (2020). https://doi.org/10.3390/nano10020376

65. J. Shen, M. Shi, N. Li, B. Yan, H. Ma, Y. Hu, M. Ye, Facile synthesis and application of Ag-chemically converted graphene nanocomposite. Nano Res. **3**, 339–349 (2010). https://doi.org/10.1007/s12274-010-1037-x

66. J. Prakash, D. Prema, K.S. Venkataprasanna, K. Balagangadharan, N. Selvamurugan, G.D. Venkatasubbu, Nanocomposite chitosan film containing graphene oxide/hydroxyapatite/gold for bone tissue engineering. Int. J. Biol. Macromol. **154**, 62–71 (2020). https://doi.org/10.1016/j.ijbiomac.2020.03.095

67. X. Sun, J. Qin, P. Xia, B. Guo, C. Yang, X. Sun, J. Qin, P. Xia, B. Guo, C. Yang, C. Song, S. Wang, Graphene oxide-silver nanoparticle membrane for biofouling control and water purification. Chem. Eng. J. **281**, 53–59 (2015). https://doi.org/10.1016/j.cej.2015.06.059

68. X. Hao, X. Wang, S. Zhou, H. Zhang, M. Liu, Microstructure and properties of silver matrix composites reinforced with Ag-doped graphene. Mater. Chem. Phys. **215**, 327–331 (2018). https://doi.org/10.1016/j.matchemphys.2018.05.036

69. H. Zhang, X. Wang, Y. Li, C. Guo, C. Zhang, Preparation and characterization of silver-doped graphene-reinforced silver matrix bulk composite as a novel electrical contact material. Appl. Phys. A. **125**, 86 (2019). https://doi.org/10.1007/s00339-019-2379-1

70. S. Zhong, B. Wang, H. Zhou, C. Li, X. Peng, Fabrication and characterization of Ag/BiOI/GO composites with enhanced photocatalytic activity. J. Alloy. Compd. **806**, 401–409 (2019). https://doi.org/10.1016/j.jallcom.2019.07.223

71. K. Hareesh, J.F. Williams, N.A. Dhole, K.M. Kodam, V.N. Bhoraskar, S.D. Dhole, Bio-green synthesis of Ag-GO, Au-GO and Ag-Au-GO nanocomposites using Azadirachta indica: Its application in SERS and cell viability. Mater. Res. Express **3**(7), 075010 (2016). https://doi.org/10.1088/2053-1591/3/7/075010

72. T. Rattana, S. Chaiyakun, N. Witit-Anun, N. Nuntawong, P. Chindaudom, S. Oaew, C. Kedkeaw, P. Limsuwan, Preparation and characterization of graphene oxide nanosheets. Proc. Eng. **32**, 759–764 (2012). https://doi.org/10.1016/j.proeng.2012.02.009

73. F. Wang, Adsorption of anionic dye on graphene nanosheets doped with ag nanoparticles: kinetics and thermodynamic study. Russ. J. Phys. Chem. A **93**, 1357–1364 (2019). https://doi.org/10.1134/S0036024419070070

74. I. Rea, M. Casalino, M. Terracciano, L. Sansone, J. Politi, L. De Stefano, Photoluminescence enhancement of graphene oxide emission by infiltration in an aperiodic porous silicon multilayer. Opt. Express **24**(21), 24413–24421 (2016). https://doi.org/10.1364/oe.24.024413

75. N.T. Lan, D.T. Chi, N.X. Dinh, N.D. Hung, H. Lan, P.A. Tuan, L.H. Thang, N.N. Trung, N.Q. Hoa, T.Q. Huy, N. Quy, T.T. Van, Duong, V.N. Phan, A.T. Le, Photochemical decoration of silver nanoparticles on graphene oxide nanosheets and their optical characterization. J. Alloy. Compd. **615**, 843–848 (2014). https://doi.org/10.1016/j.jallcom.2014.07.042

76. R. Pasricha, S. Gupta, A.K. Srivastava, A facile and novel synthesis of Ag-graphene-based nanocomposites. Small **5**(20), 2253–2259 (2009). https://doi.org/10.1002/smll.200900726

77. Y. Wang, S.S. Li, Y.C. Yeh, C.C. Yu, H.L. Chen, F.C. Li, Y.M. Chang, C.W. Chen, Interactions between fluorescence of atomically layered graphene oxide and metallic nanoparticles. Nanoscale **5**(4), 1687–1691 (2013). https://doi.org/10.1039/c2nr33220e

78. M.M. Gudarzi, F. Sharif, Enhancement of dispersion and bonding of graphene-polymer through wet transfer of functionalized graphene oxide. Express Polym. Lett. **6**(12), 1017–1031 (2012). https://doi.org/10.3144/expresspolymlett.2012.107

79. S. Kumar, S. Bose, K. Chatterjee, Amine-functionalized multiwall carbon nanotubes impart osteoinductive and bactericidal properties in poly(ε-caprolactone) composites. RSC Adv. **4**(37), 19086–19098 (2014). https://doi.org/10.1039/c4ra00875h

80. J. Ahmed, G. Luciano, I. Schizzi, Y.A. Arfat, S. Maggiore, A. Thai, Non-isothermal crystallization behavior, rheological properties and morphology of poly(ε-caprolactone)/graphene oxide nanosheets composite films. Thermochim. Acta **659**, 96–104 (2018). https://doi.org/10.1016/j.tca.2017.11.009

81. Y. Lu, W. Chen, Sub-nanometre sized metal clusters: from synthetic challenges to the unique property discoveries. Chem. Soc. Rev. **41**(9), 3594–3623 (2012). https://doi.org/10.1039/c2cs15325d

82. T. Yu, G. Wang, L. Liu, P. Wang, Z. Wei, M. Qi, Synthesis of PCL/graphene composites by in-situ polymerization. Adv. Mater. Res. **518–523**, 837–840 (2012). https://doi.org/10.4028/www.scientific.net/AMR.518-523.837

83. I. Castilla-Cortázar, A. Vidaurre, B. Marí, A.J. Campillo-Fernández, Morphology, crystallinity, and molecular weight of poly(ε-caprolactone)/graphene oxide hybrids. Polymers. **11**(7), 1099 (2019). https://doi.org/10.3390/polym11071099

84. P.B. Messersmith, E.P. Giannelis, Synthesis and barrier properties of poly(ε-caprolactone)‐layered silicate nanocomposites. J. Polym. Sci. A: Polym. Chem. **33**(7), 1047–1057 (1995). https://doi.org/10.1002/pola.1995.080330707

85. J.M. Goddard, J.H. Hotchkiss, Polymer surface modification for the attachment of bioactive compounds. Prog. Polym. Sci. **32**(7), 698–725 (2007). https://doi.org/10.1016/j.progpolymsci.2007.04.002

86. L.C. Xu, C.A. Siedlecki, Effects of surface wettability and contact time on protein adhesion to biomaterial surfaces. Biomaterials **28**(22), 3273–3283 (2007). https://doi.org/10.1016/j.biomaterials.2007.03.032

87. B.L. Gong, I.A. Kinloch, R.J. Young, I. Riaz, R. Jalil, K.S. Novoselov, Interfacial stress transfer in a graphene monolayer nanocomposite. Adv. Mater. **22**(24), 2694–2697 (2010). https://doi.org/10.1002/adma.200904264

88. L. Tang, Y. Wan, D. Yan, Y. Pei, L. Zhao, Y. Li, The effect of graphene dispersion on the mechanical properties of graphene/epoxy composites. Carbon N. Y. **60**, 16–27 (2013). https://doi.org/10.1016/j.carbon.2013.03.050

89. L.R. Jaidev, S. Kumar, K. Chatterjee, Multi-biofunctional polymer graphene composite for bone tissue regeneration that elutes copper ions to impart angiogenic, osteogenic and bactericidal properties. Colloids Surf. B: Biointerfaces **159**, 293–302 (2017). https://doi.org/10.1016/j.colsurfb.2017.07.083

90. A. Seyedsalehi, L. Daneshmandi, M. Barajaa, J. Riordan, C.T. Laurencin, Fabrication and characterization of mechanically competent 3D printed polycaprolactone-reduced graphene oxide scaffolds. Sci. Rep. **10**, 22210 (2020). https://doi.org/10.1038/s41598-020-78977-w

91. S. Mohammadi, S.S. Shafiei, M. Asadi-eydivand, M. Ardeshir, Graphene oxide-enriched poly (ε -caprolactone) electrospun nanocomposite scaffold for bone tissue engineering applications. J. Bioact. Compat. Polym. **32**(3), 325–342 (2016). https://doi.org/10.1177/0883911516668666

92. J. Tang, Q. Chen, L. Xu, S. Zhang, L. Feng, L. Cheng, H. Xu, Z. Liu, Graphene oxide-silver nanocomposite as a highly effective antibacterial agent with species-specific mechanisms. ACS Appl. Mater. Interfaces **5**(9), 3867–3874 (2013). https://doi.org/10.1021/am4005495

93. A.F. Faria, E. De, Shaulsky, L.H.A. Chavez, M. Elimelech, Antimicrobial electrospun biopolymer nano fiber mats functionalized with graphene oxide—silver nanocomposites. ACS Appl. Mater. Interfaces **7**(23), 12751–12759 (2015). https://doi.org/10.1021/acsami.5b01639

94. A.F. De Faria, D.S.T. Martinez, S.M.M. Meira, A.C.M. de Moraes, A. Brandelli, A.G.S. Filho, O.L. Alves, Anti-adhesion and antibacterial activity of silver nanoparticles supported on graphene oxide sheets. Colloids Surf. B: Biointerfaces **113**, 115–124 (2014). https://doi.org/10.1016/j.colsurfb.2013.08.006

95. J. Ma, J. Zhang, Z. Xiong, Y. Yong, X.S. Zhao, Preparation, characterization and antibacterial properties of silver-modified graphene oxide. J. Mater. Chem. **21**(10), 3350–3352 (2011). https://doi.org/10.1039/c0jm02806a

96. W.P. Xu, L.C. Zhang, J.P. Li, Y. Lu, H.H. Li, Y.N. Ma, W. Wang, S.H. Di, Yu, Facile synthesis of silver@graphene oxide nanocomposites and their enhanced antibacterial properties. J. Mater. Chem. **21**(12), 4593–4597 (2011). https://doi.org/10.1039/c0jm03376f

97. H. Ji, H. Sun, X. Qu, Antibacterial applications of graphene-based nanomaterials: recent achievements and challenges. Adv. Drug Deliv. Rev. **105**, Part B, 176–189 (2016). https://doi.org/10.1016/j.addr.2016.04.009

98. H.R. Bakhsheshi-Rad, A.F. Ismail, M. Aziz, M. Akbari, Z. Hadisi, S.M. Khoshnava, E. Pagan, X. Chen, Co-incorporation of graphene oxide/silver nanoparticle into poly-L-lactic acid fibrous: a route toward the development of cytocompatible and antibacterial coating layer on magnesium implants. Mater. Sci. Eng. C **111**, 110812 (2020). https://doi.org/10.1016/j.msec.2020.110812